



# Domain of dependence for wall-pressure measurements in high-speed boundary layers

Qi Wang<sup>1,2</sup>  and Tamer A. Zaki<sup>1</sup> 

<sup>1</sup>Mechanical Engineering, Johns Hopkins University, Baltimore, MD 21218, USA

<sup>2</sup>Aerospace Engineering, San Diego State University, San Diego, CA 92182, USA

**Corresponding author:** Tamer A. Zaki, [t.zaki@jhu.edu](mailto:t.zaki@jhu.edu)

(Received 15 July 2024; revised 2 January 2025; accepted 19 February 2025)

Measurements in high-speed flows are difficult to acquire. To maximise their utility, it is important to quantify the preceding events that can influence a sensor signal. Flow perturbations that are invisible to a sensor may prevent the detection of key physics. Conversely, perturbations that originate away from a sensor may impact its signal at the measurement time. The collection of the latter perturbations defines the domain of dependence (DOD) of the sensor, which can be evaluated efficiently using adjoint-variational methods. For Mach 4.5 transitional flat-plate boundary layers, we consider the DOD of an instantaneous and localised wall-pressure observation, akin to that by a piezoelectric probe. At progressively earlier times prior to the measurement, the DOD retreats upstream from the probe, and the sensitivity to flow perturbations expands spatially and is amplified. The expansion corresponds to a wider region where initial disturbances can influence the measurement, and the amplification is because these perturbations grow during their forward evolution before reaching the probe. The sensitivity has a wavepacket structure concentrated near the boundary-layer edge, and a portion that radiates into the free stream. The DOD is further interpreted as the optimal initial perturbation with unit energy that maximises the norm of the measurement, establishing a link to transient-growth analysis. We test this formulation for a laminar condition and contrast the sensor dependence on different components of the state vector. When the boundary layer is transitional, we adopt the general formulation to assess the impact of sensor placement within the transition and turbulent zones on the DOD, and we characterise the flow disturbances that most effectively influence the measurement in each regime.

**Key words:** boundary layer stability, compressible boundary layers

## 1. Introduction

Measurements in transitional high-speed flows are challenging to acquire due in part to the short time and length scales of the instability waves, and because some quantities are impossible to probe directly and must be evaluated from other state variables. Additionally, the sensor placement plays an important role. For example, boundary-layer measurements near the onset of linear instability may suffer from low signal-to-noise ratios while probes far downstream may be sampling the nonlinear or chaotic turbulent regime. Data-assimilation techniques have recently been demonstrated as a viable approach to interpret and augment experimental measurements using numerical simulations. The success of data assimilation, however, hinges on the extent to which measurements depend on the precursor flow events. We therefore seek to evaluate the domain of dependence of a measurement, which describes all possible earlier-in-time flow disturbances that can alter a sensor signal. In other words, the domain of dependence accounts for when, where and what perturbations can affect the measurement (Zaki 2025). In this work, we propose a framework to characterise the back-in-time domain of dependence of a measurement in high-speed flow, and to compare the sensitivity of the measurements with different components of the state vector. Our approach is based on an adjoint-variational mathematical formalism.

The difficulty of acquiring resolved spatio-temporal measurements in transitional high-speed boundary layers has motivated significant theoretical and computational activities. These efforts have largely adopted a forward perspective, attempting to predict the emergence and evolution of disturbances, and ultimately the onset of turbulence. The success of linear-stability theory for the prediction of the most unstable waves is particularly notable (Mack 1975; Malik & Spall 1991; Fedorov 2011). These methods have been extended from the study of parallel base states to spreading boundary layers (Bertolotti & Herbert 1991; Zuccher *et al.* 2006), sensitivity analyses (Park & Zaki 2019), complex geometries (Kocian *et al.* 2013; Moyes & Reed 2019) and nonlinear effects (Chang *et al.* 1991, 1993). To predict transition to the fully turbulent state, direct numerical simulations (DNS) are considered the highest fidelity approach. While DNS are computationally costly, they are feasible since the range of scales in the transitional regime can be resolved at relevant Mach and Reynolds numbers. The challenge in forward approaches lies in how to prescribe initial and boundary conditions, which have a significant impact on the downstream flow dynamics, including the amplification of instability waves, their nonlinear interactions and the particular transition scenario that is realised. Previous efforts have examined canonical transition mechanisms, for example by simulating a primary wave and its secondary instability through fundamental or sub-harmonic resonance (Franko & Lele 2014; Hader & Fasel 2019). A qualitatively different approach adopted by Hader & Fasel (2018) was to introduce white-noise forcing in order to initiate boundary-layer instabilities. A third strategy is to perform tunnel-scale computations in order to account for the noise from the boundary layers entering the test section (Duan *et al.* 2019), although this strategy is quite costly and is not applicable to flight tests.

Experiments also examine the forward flow evolution. For example, gas in a high-pressure tank is expanded in a Ludwieg tube to instantiate flow over the test article (Kimmel *et al.* 2017; Kennedy *et al.* 2022). The experimentalist is faced with unique challenges associated with characterisation of the flow environment and the limitations imposed by available measurement techniques (Parziale *et al.* 2014; Hofferth & Ogg 2019; Kostak *et al.* 2019; Mamrol & Jewell 2022). In addition, the acquired sensor data must be

interpreted in order to extract, or at times infer, quantities of interest. For example, the finite sensor size of a picoCoulomb (PCB) probe has a filtering effect (Kennedy *et al.* 2018), and hence corrections must be adopted when evaluating spectra (Corcos 1963; Lueptow 1995). When the amplitudes of disturbances upstream of the first sensor is of interest, it must be estimated using a model (Marineau *et al.* 2014). In the context of schlieren imaging, Kennedy *et al.* (2018) adopted a form of Taylor hypothesis to construct a time series from temporally under-resolved but spatially resolved measurements. Later efforts utilised an ultra-high frame rate imaging to resolve the flow (Butler & Laurence 2021, 2022), and the images are then processed to extract characteristics of the instability waves. For complex geometries, measurements from different modalities (e.g. PCB sensors, infrared thermography, etc.) are combined to construct a more complete description of the flow (Berridge *et al.* 2019; Kostak & Bowersox 2021). Interpretation of the measurements can, however, be obscured by uncertainties (Schneider 2015).

The interpretation of measurements can be regarded as the inverse, or observer, perspective, where one starts from probe data and attempts to identify the origin of the observations. A rigorous mathematical framework for such interpretation is data assimilation (Law *et al.* 2015; Asch *et al.* 2016), which attempts to reduce uncertainty by exploiting the measurements themselves. The basic idea is to use the sensor data as targets during the search for uncertain simulation parameters, such that the computations can reproduce the measurements (Zaki & Wang 2021). Once the unknown simulation parameters are discovered, the computational predictions provide a complete description of the flow, beyond the original sensor data. Data assimilation can thus augment spatio-temporally under-resolved measurements (Li *et al.* 2020; Du *et al.* 2023), estimate unknown parameters (Mons *et al.* 2016, 2021), predict quantities of interest that cannot be directly measured (Loose & Heimbach 2021; Clark Di Leoni *et al.* 2023) or forecast the dynamics beyond the measurement horizon (Stammer *et al.* 2016). The simulations themselves attain a level of fidelity that is not possible without the measurements. These ideas are actively being pursued in basic research related to transitional (Buchta & Zaki 2021) and turbulent flows (Wang & Zaki 2021). Applications to high-speed transitional flows have demonstrated the capacity of these techniques to estimate the entire flow field from wall-pressure data from Mach 6 flow over a cone (Buchta *et al.* 2022).

The success of the assimilation directly hinges on the dependence of available measurements on the unknown parameters, for example, the dependence of downstream measurements in a boundary layer on upstream events in the flow. It is important to determine where, when and what flow perturbations would impact a specific observation, or in other words, analyse the domain of dependence (DOD) of the measurement data. The adjoint to the forward governing equations are an efficient approach to evaluate sensitivities (Lockwood & Mavriplis 2010; Poulain *et al.* 2024), and will be adopted herein to evaluate the DOD of a measurement as a function of backward time. This idea was briefly introduced for a wall-stress measurement in incompressible flow (Wang *et al.* 2022), but has not been pursued in depth or in the context of high-speed flows. The notion of a measurement DOD in compressible flow is mathematically more nuanced and involves unique physics, for example due to the distinction between acoustic, vortical and entropic disturbances. In transitional hypersonic boundary layers, surface measurements are commonly performed and used to characterise the flow state. However, it is difficult to unambiguously differentiate the sensitivity of the measurements to potential upstream and earlier in time events. In addition, some upstream disturbances may not at all influence a wall-pressure sensor, or may only do so indirectly through the dynamics of its evolution to the sensor location at the measurement time.

The idea of the DOD of a measurement can be helpful in the design of measurement campaigns, as it can provide guidance regarding which quantities to monitor, where to place sensors and how to interpret the data effectively (Wheaton *et al.* 2021). For instance, the DOD can identify regions of the flow and types of disturbances that have the most significant influence on the sensor data. This knowledge can then be used to target these effects, thereby improving the accuracy and reliability of the data. Recent examples from data assimilation have also demonstrated that sensor placement can be optimised to reduce the uncertainty in the solution of the data-assimilation problem (Mons *et al.* 2019; Buchta & Zaki 2021).

The present work introduces the formulation of the DOD of a point observation in high-speed boundary layers, using an adjoint-variational method. A schematic representation is provided in figure 1, which compares the conventional forward and herein formulated adjoint approach. In the former, a new computation or experiment is required to assess the influence a disturbance on the sensor. In contrast, using a single adjoint computation, we can define the DOD of the sensor and the influence of any potential disturbance on the measurement. The adjoint approach thus provides significant computational efficiency, without the requirement for multiple forward simulations or optimisation of a cost function as usually encountered in data-assimilation problems. A wall-pressure measurement is used as an example to develop and demonstrate the approach. Three positions within the development of the flow are considered: (a) the early laminar regime; (b) the nonlinear regime preceding transition; (c) the turbulent region. The structure of the paper is designed as follows. In § 2, we develop the mathematical formulation. In § 3.1, we present results in the laminar region, for a parallel boundary layer. In § 3.3, the analysis is performed for the spatial boundary layer, and the three sensor placements are contrasted.

## 2. Theoretical formulation

The DOD of a sensor that is placed in high-speed flow has significant implications for our capacity to interpret the measurement. In this section, we introduce the theoretical formulation to characterise an isolated measurement, and adopt wall pressure as a demonstrative example. However, the formulation is kept general and applicable to other types of measurements. In order to motivate our approach, we briefly note how measurements feature in data assimilation, although we do not perform the assimilation in this work.

The flows of interest are governed by the compressible Navier–Stokes equations. To aid the presentation, we consider a flat-plate boundary layer as shown schematically in figure 1. Three regimes are qualitatively distinguished – laminar, transitional and turbulent – which can be quantitatively demarcated, e.g. based on the wall-friction coefficient. We adopt the Blasius length as a reference scale  $L^* = \sqrt{x_0^* \mu_\infty^* / (\rho_\infty^* U_\infty^*)}$ , where  $x_0^*$  is the streamwise location at the inflow. The other reference quantities are the free-stream values of density  $\rho_\infty^*$ , viscosity  $\mu_\infty^*$ , conductivity  $\kappa_\infty^*$ , temperature  $T_\infty^*$  and velocity  $U_\infty^*$ . Using these scales, the non-dimensional governing equations are

$$\begin{aligned} \frac{\partial \rho}{\partial t} + \nabla \cdot (\rho \mathbf{u}) &= 0, \\ \frac{\partial \rho \mathbf{u}}{\partial t} + \nabla \cdot (\rho \mathbf{u} \mathbf{u}) &= -\nabla p + \nabla \cdot \boldsymbol{\tau}, \\ \frac{\partial E}{\partial t} + \nabla \cdot (\mathbf{u} (E + p)) &= \nabla \cdot (\boldsymbol{\tau} \cdot \mathbf{u}) + \frac{\gamma}{(\gamma - 1) Re Pr} \nabla \cdot (\kappa \nabla T), \end{aligned} \tag{2.1}$$

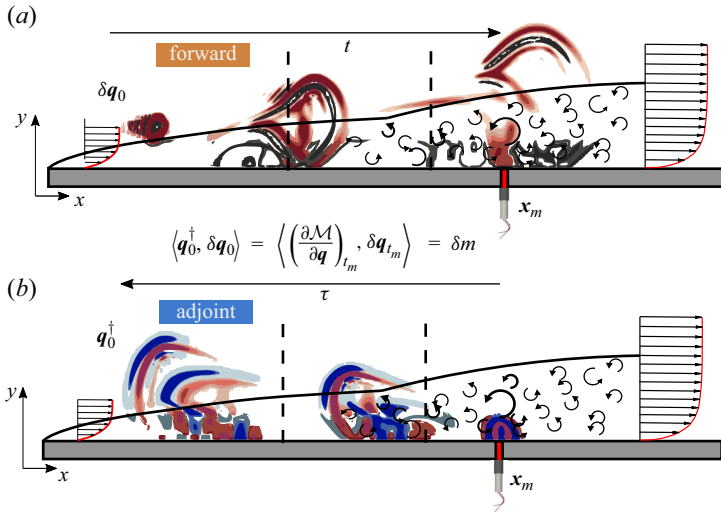


Figure 1. Schematic of the domain of influence and the DOD in a spatially developing transitional boundary layer. The dashed lines separate the laminar, transitional and turbulent regions within the flow. Here,  $x_m$  marks the location of the pressure sensor. Schematics of the forward perturbation and adjoint evolutions of the flow field are shown on the top and bottom. The forward-adjoint duality relation between them shows the physical interpretation of adjoint, i.e. the DOD.

where

$$\boldsymbol{\tau} = \frac{1}{Re} \mu \left( \nabla \mathbf{u} + (\nabla \mathbf{u})^\top \right) + \frac{1}{Re} \left( \mu_b - \frac{2}{3} \mu \right) (\nabla \cdot \mathbf{u}) \mathbf{I}, \quad (2.2)$$

$$E = \frac{\rho}{\gamma(\gamma - 1)M^2} T + \frac{1}{2} \rho \|\mathbf{u}\|^2, \quad (2.3)$$

and the equation of state is

$$p = \rho RT = \rho T / (\gamma M^2). \quad (2.4)$$

The Reynolds number based on the Blasius length scale is  $Re = \rho_\infty^* U_\infty^* L^* / \mu_\infty^*$ , and that based on streamwise position is  $Re_x = \rho_\infty^* U_\infty^* x^* / \mu_\infty^*$ . The two are related at the starting position of the domain,  $Re = \sqrt{Re_{x_0}}$ . The Mach and Prandtl numbers are defined by  $M = U_\infty^* / a_\infty^* = U_\infty^* / \sqrt{\gamma R^* T_\infty^*}$  and  $Pr = \mu_\infty^* C_{p,\infty}^* / \kappa_\infty^*$ , where  $\gamma = 1.4$  is the ratio of specific heats for air, and  $C_{p,\infty}^*$  is the free-stream specific heat at constant pressure. The relationship between the viscosity and the temperature is modelled by the power law  $\mu = T^n$ , with  $n = 0.983$  as a fit for Sutherland’s law. The flow state can be expressed in terms of primitive variables,  $\mathbf{q} = [\rho, \mathbf{u}, T]^\top$ , or conserved quantities,  $\mathbf{s} = [\rho, \rho \mathbf{u}, E]^\top$ . The governing equations (2.1) can then be written compactly as  $\mathbf{q}(t) = \mathcal{N}(\mathbf{q}_0)$ , where  $\mathcal{N}$  is the compressible Navier–Stokes operator that maps the initial condition  $\mathbf{q}_0$  to the state  $\mathbf{q}(t)$  at time  $t$ .

In general, the measurements  $\mathbf{m}$  can be expressed as  $\mathbf{m} = \mathcal{M}(\mathbf{q}_{t_m})$ , where  $\mathcal{M}$  is a linear or nonlinear observation operator acting on  $\mathbf{q}$ , and  $t_m$  is the measurement time. For example, if the pressure at a sensor position is of interest, the operator  $\mathcal{M}$  extracts a single-point pressure measurement and is defined as

$$\mathcal{M}(\mathbf{q}_{t_m}) = \int_V p(\mathbf{x}, t_m) \delta(\mathbf{x} - \mathbf{x}_m) dV. \quad (2.5)$$

The measurements can then be related to the initial state  $\mathbf{q}_0$  according to

$$\mathbf{m} = \mathcal{M}(\mathcal{N}(\mathbf{q}_0)), \tag{2.6}$$

which highlights that a modification in  $\mathbf{q}_0$  can alter  $\mathbf{m}$ .

The assimilation of experimental data in simulations can be formulated as a nonlinear optimisation. One then searches for the initial flow state  $\mathbf{q}_0$  whose nonlinear evolution optimally reproduces available experimental data  $\mathbf{m}_e$ . The cost function of this optimisation is therefore defined in terms of the difference between the estimated and true observations

$$J(\mathbf{q}_0) = \frac{1}{2} \|\mathbf{m} - \mathbf{m}_e\|^2 = \frac{1}{2} \|\mathcal{M}(\mathcal{N}(\mathbf{q}_0)) - \mathbf{m}_e\|^2, \tag{2.7}$$

which must be minimised; the notation  $\|\bullet\|$  indicates vector norm in Euclidean space. Evidently, the solution of the data-assimilation problem depends on the gradient of  $J$  with respect to  $\mathbf{q}_0$ , or the sensitivity of the measurements to variations in the initial flow state. While this gradient vanishes at optimality, it must be finite away from the true solution for the data assimilation to be successful. Conversely, if the observations are not sensitive to changes in the flow state, it is futile to attempt the optimisation problem.

### 2.1. Measurement domain of dependence

While  $\mathbf{m}$  typically comprises multiple observations, the analysis benefits from isolating a single measurement that is denoted by the scalar  $m$ . This focused approach allows more precise characterisation of an individual measurement, and can be repeated for an ensemble of observations. The derivation of the measurement DOD starts by perturbing the initial state and evaluating the change in the cost function (2.7). In this regard, the DOD is equivalent to the sensor sensitivity which is the terminology adopted in data assimilation where the objective is to minimise the cost. As such, both terms can be used interchangeably, although we prefer ‘domain of dependence’ because we are not concerned with cost minimisation but rather characterisation of the sensor itself. Using the Fréchet derivative, the variation in the cost is given as

$$\begin{aligned} \delta J &= [\mathcal{M}(\mathcal{N}(\mathbf{q}_0)) - m_e] \left\langle \left( \frac{\partial \mathcal{M}}{\partial \mathbf{q}} \right)_{t_m}, \delta \mathbf{q}_{t_m} \right\rangle \\ &= [\mathcal{M}(\mathcal{N}(\mathbf{q}_0)) - m_e] \left\langle \left( \frac{\partial \mathcal{M}}{\partial \mathbf{q}} \right)_{t_m}, \mathcal{L}_q \delta \mathbf{q}_0 \right\rangle. \end{aligned} \tag{2.8}$$

The inner product in (2.8) follows the definition of Chu’s energy (Chu 1965; Hanifi *et al.* 1996), which is designed to include both kinetic and potential energy from compression and heat exchange, with appropriate coefficients to exclude the effect of conservative compression. This form of energy guarantees a monotonically non-increasing total energy in a uniform, homogeneous medium at rest. This energy inner product can be expressed as

$$\begin{aligned} \langle \delta \mathbf{q}_1, \delta \mathbf{q}_2 \rangle &= \int_{\mathcal{V}} \delta \mathbf{q}_1^\top \boldsymbol{\Xi} \delta \mathbf{q}_2 \, d\mathcal{V} \\ &= \frac{1}{2} \int_{\mathcal{V}} \left[ R \frac{\bar{T}}{\bar{\rho}} \delta \rho_1 \delta \rho_2 + \bar{\rho} \delta \mathbf{u}_1 \cdot \delta \mathbf{u}_2 + \frac{R}{\gamma - 1} \frac{\bar{\rho}}{\bar{T}} \delta T_1 \delta T_2 \right] \, d\mathcal{V}, \end{aligned} \tag{2.9}$$

where  $\bar{\rho}$  and  $\bar{T}$  are averaged quantities. In a developing boundary layer, averaging is performed in the spanwise direction and in time, which can be denoted as  $\bar{\mathbf{q}} = \bar{\mathbf{q}}^{z,t}$ .

The matrix  $\Xi$  contains the weights that are required to calculate the total energy from the perturbation state vectors. The energy norm is most conveniently formulated in terms of the primitive variables,  $\mathbf{q} = [\rho, \mathbf{u}, T]^\top$ . When conserved variables  $\mathbf{s} = [\rho, \rho\mathbf{u}, E]^\top$  are adopted, the associated weight matrix must be adopted, which can be derived from the transformation between state vectors (see Appendix A).

The term  $(\partial\mathcal{M}/\partial\mathbf{q})_{t_m}$  will be referred to as the measurement kernel. In order to clarify its nature, we consider the example of a pressure measurement, where  $p = \rho T/(\gamma M^2)$ . The derivative of the measurement operator with respect to the flow state, at the measurement time  $t_m$ , is given by

$$\left(\frac{\partial\mathcal{M}}{\partial\mathbf{q}}\right)_{t_m} = 2 \left[ \frac{T}{\bar{T}} \bar{\rho}, 0, 0, 0, (\gamma - 1) \frac{\rho}{\bar{\rho}} \frac{\bar{T}}{T} \right]^\top \delta(\mathbf{x} - \mathbf{x}_m). \tag{2.10}$$

This expression is different from taking the derivative of pressure with respect to the primitive variables. Instead, it is the Fréchet derivative that takes into account the weight matrix in the definition of the inner product, namely  $\delta m = \langle (\partial\mathcal{M}/\partial\mathbf{q})_{t_m}, \delta\mathbf{q}_{t_m} \rangle$ .

The last equality in (2.8) introduced the linearised Navier–Stokes operator  $\mathcal{L}_q$ , where the linearisation is performed around the base solution, i.e.

$$\delta\mathbf{q}_{t_m} = \mathcal{N}(\mathbf{q}_0 + \delta\mathbf{q}_0) - \mathcal{N}(\mathbf{q}_0) = \mathcal{L}_q \delta\mathbf{q}_0, \tag{2.11}$$

for a small initial perturbation  $\delta\mathbf{q}_0$ . Using integration by parts, we can write (2.8) as

$$\begin{aligned} \delta J &= [\mathcal{M}(\mathcal{N}(\mathbf{q}_0)) - m_e] \left\langle \left(\frac{\partial\mathcal{M}}{\partial\mathbf{q}}\right)_{t_m}, \mathcal{L}_q \delta\mathbf{q}_0 \right\rangle \\ &= [\mathcal{M}(\mathcal{N}(\mathbf{q}_0)) - m_e] \left\langle \mathcal{L}_q^\dagger \left(\frac{\partial\mathcal{M}}{\partial\mathbf{q}}\right)_{t_m}, \delta\mathbf{q}_0 \right\rangle, \end{aligned} \tag{2.12}$$

where  $\mathcal{L}_q^\dagger$  represents solving the adjoint equations. The gradient, or Fréchet derivative, of the cost with respect to the initial state is therefore

$$\frac{\partial J}{\partial\mathbf{q}_0} = [\mathcal{M}(\mathcal{N}(\mathbf{q}_0)) - m_e] \mathcal{L}_q^\dagger \left(\frac{\partial\mathcal{M}}{\partial\mathbf{q}}\right)_{t_m} = [\mathcal{M}(\mathcal{N}(\mathbf{q}_0)) - m_e] \mathbf{q}_0^\dagger. \tag{2.13}$$

The last equality is the adjoint map

$$\mathbf{q}_0^\dagger = \mathcal{L}_q^\dagger \left(\frac{\partial\mathcal{M}}{\partial\mathbf{q}}\right)_{t_m} = \mathcal{L}_q^\dagger \mathbf{q}_{t_m}^\dagger, \tag{2.14}$$

which represents solving the adjoint equations backward in time, from  $t = t_m$  to  $t = 0$ . Specifically, starting from the measurement kernel,  $\mathbf{q}_{t_m}^\dagger = (\partial\mathcal{M}/\partial\mathbf{q})_{t_m}$ , the adjoint equations are evolved back in time to obtain  $\mathbf{q}_0^\dagger$ , which for our purposes is the most important contribution to the gradient of the cost function (2.13).

It is clear from (2.13) that the gradient of the cost function vanishes at the true solution  $\mathbf{q}_0 = \mathbf{q}_{0,e}$ , since  $\mathcal{M}(\mathcal{N}(\mathbf{q}_{0,e})) = m_e$ . One interesting implication is that the properties of the cost function at optimality are encapsulated in its Hessian

$$\begin{aligned} \frac{\partial^2 J}{\partial\mathbf{q}_0 \partial\mathbf{q}_0} &= \left( \mathcal{L}_q^\dagger \left(\frac{\partial\mathcal{M}}{\partial\mathbf{q}}\right)_{t_m} \right) \left( \mathcal{L}_q^\dagger \left(\frac{\partial\mathcal{M}}{\partial\mathbf{q}}\right)_{t_m} \right) + \underbrace{[\mathcal{M}(\mathcal{N}(\mathbf{q}_{0,e})) - m_e]}_{=0} \mathcal{L}_q^\dagger \mathcal{L}_q^\dagger \frac{\partial^2 \mathcal{M}}{\partial\mathbf{q}_{t_m} \partial\mathbf{q}_{t_m}} \\ &= \mathbf{q}_0^\dagger \mathbf{q}_0^\dagger. \end{aligned} \tag{2.15}$$

In other words, at the special optimal state, the Hessian matrix is the cross-correlation of the initial adjoint field which is generated from the observation kernel (Wang *et al.* 2022).

We now return to the general meaning of the adjoint state, not necessarily at optimality. An important interpretation of the adjoint field is that it measures the sensitivity of the measurement to a perturbation in the initial condition. To highlight this connection, consider an infinitesimal deviation in the initial state  $\delta\mathbf{q}_0$ . The associated perturbation in the measurement is

$$\delta m = \left\langle \left( \frac{\partial \mathcal{M}}{\partial \mathbf{q}} \right)_{t_m}, \delta \mathbf{q}_{t_m} \right\rangle = \left\langle \left( \frac{\partial \mathcal{M}}{\partial \mathbf{q}} \right)_{t_m}, \mathcal{L}_q \delta \mathbf{q}_0 \right\rangle, \quad (2.16)$$

which we re-write in terms of the adjoint field according to

$$\delta m = \left\langle \mathcal{L}_q^\dagger \left( \frac{\partial \mathcal{M}}{\partial \mathbf{q}} \right)_{t_m}, \delta \mathbf{q}_0 \right\rangle = \left\langle \mathbf{q}_0^\dagger, \delta \mathbf{q}_0 \right\rangle. \quad (2.17)$$

This expression relates perturbations to the initial condition  $\delta\mathbf{q}_0$  to variations in the observation at the sensing location and time,  $\delta m$ . In other words, the adjoint field at the initial time is the sensor sensitivity,  $\mathbf{q}_0^\dagger = \partial m / \partial \mathbf{q}_0$ . Taken together, (2.16) and (2.17) define the forward-adjoint duality relation

$$\delta m = \left\langle \left( \frac{\partial \mathcal{M}}{\partial \mathbf{q}} \right)_{t_m}, \mathcal{L}_q \delta \mathbf{q}_0 \right\rangle = \left\langle \mathbf{q}_0^\dagger, \delta \mathbf{q}_0 \right\rangle. \quad (2.18)$$

The schematic in figure 1 illustrates the above relations, (2.16) and (2.17), and the notation of duality (2.18). To evaluate a deviation in the measurement  $\delta m$  without the aid of the adjoint, numerous forward computations must be performed, one for each perturbation  $\delta\mathbf{q}_0$  (2.16). This approach is computationally costly, and becomes intractable for very high-dimensional problems. In contrast, (2.17) shows that the same  $\delta m$  can be predicted for any initial disturbance using a simple inner product with a particular adjoint field. This specific adjoint is the back-in-time evolution from the measurement kernel, and the associated computational cost is a single adjoint simulation. Once  $\mathbf{q}_0^\dagger$  is obtained, it can be regarded as the Riesz vector linking the perturbations in the measurement and in the initial flow state. Perturbations outside the support of the adjoint field at  $t = 0$  or within it but orthogonal to  $\mathbf{q}_0^\dagger$  have no impact on the sensor at the measurement time. Conversely, only measurements within the support of  $\mathbf{q}_0^\dagger$  and with a finite projection onto this field can alter the sensor signal at the measurement time. The most effective initial disturbance in this regard is one that is aligned with the adjoint field. This adjoint field thus defines the sensitivity of the sensor to the antecedent flow events, or its DOD.

The duality relation (2.18) is foundational to the solution of inverse problems, or data assimilation. Consider for example two perturbations that have the same inner product with the adjoint field; they will yield the same impact on the sensor signal at the measurement time, and are thus indistinguishable by a single probe. This examples exposes the potential non-uniqueness of the solution of the inverse problem and the benefit of employing diverse sensor modalities. Our interest in the present work is not, however, data assimilation. Instead, our primary focus is on the interpretation of the adjoint field that is initiated from the measurement kernel as the sensor DOD.

The adjoint equations are notably dependent on the choice of state variables and the specific definition of the inner product. For example, the adjoint equations may be derived

from conserved variables and using a standard dot product (e.g. Vishnampet Ganapathi Subramanian 2015)

$$[s_1, \mathcal{L}_s s_2] = \int_{\mathcal{V}} s_1^\top \mathcal{L}_s s_2 d\mathcal{V} = \int_{\mathcal{V}} \left( \mathcal{L}_s^\dagger s_1 \right)^\top s_2 d\mathcal{V} = \left[ \mathcal{L}_s^\dagger s_1, s_2 \right]. \quad (2.19)$$

Here, the square brackets denote a standard dot product without any additional weighting. The adjoint operators  $\mathcal{L}_q^\dagger$  in (2.16) and  $\mathcal{L}_s^\dagger$  in the above equation are different, and so are their associated adjoint variables. The relation between the two definitions of the adjoint is provided in Appendix A.

### 2.2. Eigen-representation of measurement domain of dependence

The above formulation of sensor sensitivity is general, and can be adopted with any type of measurement and in complex flow configurations. In canonical flows, for example a flat-plate laminar boundary layer, the formulation can be expressed in the language of linear-stability theory (LST). Here, we will demonstrate this connection in the temporal setting, where the boundary layer is assumed to be locally parallel, and the perturbations evolve in time. The adjoint evolution (2.14) thus becomes an initial value problem starting from the measurement kernel,  $q_{t_m}^\dagger = (\partial \mathcal{M} / \partial q)_{t_m}$ . The solution can be expressed in terms of an appropriate basis, for example the eigenfunctions of the temporal linear-stability operator or its adjoint. For brevity, we only show the formulation for the former choice, which is sufficient and eliminates the dependence on constructing an accurate adjoint solver that satisfies the forward-adjoint duality relation.

With the locally parallel assumption for the base flow, we can adopt a Fourier representation of variables in the homogeneous streamwise and spanwise directions

$$\begin{aligned} \delta q_0(x) &= \int_{k_z} \int_{k_x} \delta \hat{q}_0(y, k_x, k_z) e^{ik_x x} e^{ik_z z} dk_x dk_z, \\ q_0^\dagger(x) &= \int_{k_z} \int_{k_x} \hat{q}_0^\dagger(y, k_x, k_z) e^{ik_x x} e^{ik_z z} dk_x dk_z. \end{aligned} \quad (2.20)$$

We will restrict our attention to a single horizontal wavenumber vector  $\kappa = (k_x, k_z)$ , and omit these arguments to simplify the notation. We further expand the wall-normal profiles,  $\delta \hat{q}_0(y)$  and  $\hat{q}_0^\dagger(y)$ , in terms of the eigenfunctions  $\tilde{q}(y)$  of the forward temporal-stability problem

$$\begin{aligned} \delta \hat{q}_0(y) &= \sum_n a_n \tilde{q}^{(n)}(y) + \int_\omega a_\omega \tilde{q}^{(\omega)}(y) d\omega, \\ \hat{q}_0^\dagger(y) &= \sum_n b_n \tilde{q}^{(n)}(y) + \int_\omega b_\omega \tilde{q}^{(\omega)}(y) d\omega. \end{aligned} \quad (2.21)$$

The summation is performed over the discrete modes, and the integration is over the continuous branches parameterised by  $\omega$ , where  $d\omega$  represents the measure associated with the continuous branch on the  $\omega$  plane. Numerical evaluation of the linear-stability eigen-modes is influenced by domain height and grid resolution (Fedorov & Tumin 2011; Poulain *et al.* 2024), and must therefore be verified for convergence. The coefficients in the above expansions are denoted  $a$  and  $b$ , for the forward and adjoint states, respectively. The dependence of the eigenmodes ( $\tilde{q}, \omega$ ) and of the coefficients ( $a, b$ ) on the wavenumber  $\kappa$  is implicit in the above expressions. Substituting the expansion of the initial perturbation  $\delta \hat{q}_0(y)$  in the linearised forward equations, and using the bi-orthogonality of

the eigenfunctions, we can derive the following expression for the forward field at the measurement time  $t_m$ :

$$\delta\hat{\mathbf{q}}(y, t_m) = \hat{\mathcal{L}}_q \delta\hat{\mathbf{q}}_0 = \sum_n a_n e^{-i\omega_n t_m} \tilde{\mathbf{q}}^{(n)}(y) + \int_{\omega} a_{\omega} e^{-i\omega t_m} \tilde{\mathbf{q}}^{(\omega)}(y) d\omega. \quad (2.22)$$

The analytical expression involves all the discrete and continuous-branch modes. Numerically, a finite number of modes are retained and the eigenfunctions are arranged as the column vectors of matrix  $\tilde{\mathbf{Q}}$ . In the discrete form, the forward perturbation at the initial and measurement times ( $\delta\hat{\mathbf{q}}_0$  and  $\delta\hat{\mathbf{q}}_{t_m}$ ), and the adjoint field  $\hat{\mathbf{q}}_0^{\dagger}(y)$ , are represented as

$$\delta\hat{\mathbf{q}}_0(y) = \tilde{\mathbf{Q}}\mathbf{a}, \quad \delta\hat{\mathbf{q}}(y, t_m) = \tilde{\mathbf{Q}}\Lambda^{t_m}\mathbf{a}, \quad \hat{\mathbf{q}}_0^{\dagger}(y) = \tilde{\mathbf{Q}}\mathbf{b}, \quad (2.23)$$

where  $\Lambda$  is a diagonal matrix with elements  $e^{-i\omega}$ .

We substitute the above expressions in the spectral form of forward-adjoint duality (2.18)

$$\delta\hat{m} = \left\langle \left( \frac{\partial \mathcal{M}}{\partial \mathbf{q}} \right)_{t_m}, \hat{\mathcal{L}}_q \delta\hat{\mathbf{q}}_0 \right\rangle = \langle \hat{\mathbf{q}}_0^{\dagger}, \delta\hat{\mathbf{q}}_0 \rangle, \quad (2.24)$$

and obtain

$$\mathbf{O}\Lambda^{t_m}\mathbf{a} = \mathbf{b}^H \mathbf{G}\mathbf{a}. \quad (2.25)$$

The matrix  $\mathbf{O}$  has  $j$  columns, each corresponding to the observations  $\mathbf{o}_j = \langle \partial \mathcal{M} / \partial \mathbf{q}_{t_m}, \tilde{\mathbf{q}}_j \rangle$  evaluated from the  $j$ -eigenfunction. In the case of one observation, e.g. when observing the wall pressure at time  $t_m$ , matrix  $\mathbf{O}$  has a single row with  $O_{1j} = \tilde{p}_j|_{wall}$ . The matrix  $G_{ij} = \langle \tilde{\mathbf{q}}_i, \tilde{\mathbf{q}}_j \rangle$  is the Grammian, evaluated using the energy inner product of each pair of forward eigenmodes. Equation (2.25) is true for any arbitrary choice of the initial disturbance, and hence any choice of  $\mathbf{a}$ . As a result

$$\mathbf{b} = \mathbf{G}^{-1} (\Lambda^{t_m})^H \mathbf{O}^H, \quad (2.26)$$

and the adjoint field can be evaluated from

$$\hat{\mathbf{q}}_0^{\dagger} = \tilde{\mathbf{Q}}\mathbf{G}^{-1} (\Lambda^{t_m})^H \mathbf{O}^H. \quad (2.27)$$

The above representation of the adjoint fields can be related to the theory of non-modal, or transient, energy amplification from linear-stability analysis. In the original transient-growth formulation, we seek the optimal initial perturbation with unit energy, which maximises the energy  $\mathcal{E} = 1/2 \|\delta\hat{\mathbf{q}}\|_E^2 = 1/2 \langle \delta\hat{\mathbf{q}}, \delta\hat{\mathbf{q}} \rangle$  at a target time. In a similar vein, we can seek the optimal initial perturbation with unit energy that maximises the change in the measurement

$$\frac{1}{2} |\delta\hat{m}|^2 = \frac{1}{2} \left\langle \left( \frac{\partial \mathcal{M}}{\partial \mathbf{q}} \right)_{t_m}, \hat{\mathcal{L}}_q \delta\hat{\mathbf{q}}_0 \right\rangle^2 = \frac{1}{2} \mathbf{a}^H (\Lambda^{t_m})^H \mathbf{O}^H \mathbf{O} \Lambda^{t_m} \mathbf{a}, \quad (2.28)$$

which is equivalent to maximising

$$\max_{\delta\hat{\mathbf{q}}_0} \frac{\frac{1}{2} |\delta\hat{m}|^2}{\|\delta\hat{\mathbf{q}}_0\|_E^2} = \frac{1}{2} \max_{\alpha} \frac{\mathbf{a}^H (\Lambda^{t_m})^H \mathbf{O}^H \mathbf{O} \Lambda^{t_m} \mathbf{a}}{\mathbf{a}^H \mathbf{G} \mathbf{a}}. \quad (2.29)$$

Using a Cholesky decomposition of  $\mathbf{G} = \mathbf{F}\mathbf{F}^H$ , we write

$$\begin{aligned} \max_{\delta\hat{\mathbf{q}}_0} \frac{\frac{1}{2}|\delta\hat{m}|^2}{\|\delta\hat{\mathbf{q}}_0\|_E^2} &= \frac{1}{2} \max_{\alpha} \frac{\mathbf{a}^H \mathbf{F}\mathbf{F}^{-1} (\mathbf{A}^{t_m})^H \mathbf{O}^H \mathbf{O} \mathbf{A}^{t_m} \mathbf{F}^{-H} \mathbf{F}^H \mathbf{a}}{\mathbf{a}^H \mathbf{F}\mathbf{F}^H \mathbf{a}} \\ &= \frac{1}{2} \max_{\alpha} \frac{\|\mathbf{O} \mathbf{A}^{t_m} \mathbf{F}^{-H} \mathbf{F}^H \mathbf{a}\|^2}{\|\mathbf{F}^H \mathbf{a}\|^2} = \frac{1}{2} \|\mathbf{O} \mathbf{A}^{t_m} \mathbf{F}^{-H}\|^2. \end{aligned} \tag{2.30}$$

When  $\mathbf{O}$  has multiple rows (multiple measurements), the above formulation requires singular value decomposition of the matrix  $\mathbf{O} \mathbf{A}^{t_m} \mathbf{F}^{-H}$ . When only one measurement is taken,  $\mathbf{O}$  has one row, and the maximum variation in the observation is achieved when  $\mathbf{F}^H \mathbf{a}$  is aligned with  $(\mathbf{O} \mathbf{A}^{t_m} \mathbf{F}^{-H})^H$ . Equivalently, the optimal coefficients, which we denote  $\mathbf{a}_0$ , are chosen such that

$$\mathbf{F}^H \mathbf{a}_0 \propto (\mathbf{O} \mathbf{A}^{t_m} \mathbf{F}^{-H})^H, \tag{2.31}$$

and therefore

$$\mathbf{a}_0 \propto \mathbf{G}^{-1} (\mathbf{A}^{t_m})^H \mathbf{O}^H = \mathbf{b}, \tag{2.32}$$

which agrees with (2.27).

Expressed in the language of optimal transient growth, the adjoint field associated with the measurement kernel is the optimal direction for the initial perturbation to maximally influence the measurement. The derivation demonstrated the equivalence for a single observation data, and is straightforward to generalise when multiple observations are provided and  $\mathbf{O}$  has multiple rows. Another benefit of using this formulation is that we can obtain the coefficients  $\mathbf{a}_0$  when projecting the adjoint sensitivity onto the forward modes. The results are identical to invoking the bi-orthogonality condition between the forward and adjoint eigenmodes.

This formulation is introduced to establish a connection to the existing linear-stability literature and applications in canonical flows. For complex configurations, e.g. transitional boundary layers or complex geometries, the original form of the measurement DOD that was introduced in § 2.1, e.g. (2.18), should be adopted.

### 3. Results

The DOD of a measurement, for example from a wall-pressure probe, naturally depends on the flow within which the sensor is placed. We will adopt high-speed, zero-pressure-gradient, laminar and transitional boundary layers as base states, and consider a wall-pressure measurement in order to demonstrate the ideas introduced in the previous section. The free-stream Mach number is  $M = 4.5$ , and the Reynolds numbers span the range  $1800 \leq \sqrt{Re_x} \leq 2800$ . We start with a qualitative discussion based on the transitional case and then take a step back to analyse a simpler laminar parallel boundary layer, and lastly return to the more complex transitional flow.

The base flows are computed using direct numerical simulations (Vishnampet *et al.* 2015), and the adjoint computations are performed using the discrete-adjoint approach in order to ensure that duality relations are satisfied to machine precision (Vishnampet *et al.* 2015; Wang *et al.* 2019). The flow domains are three-dimensional rectangular boxes, with periodic boundary conditions in the spanwise direction ( $z$ ). At the bottom surface, iso-thermal and no-slip conditions are enforced. The hot wall temperature is prescribed at 4.21 times the edge value, which is similar to the adiabatic wall temperature. At the top boundary, a far-field pressure condition with a sponge region is adopted, where the state is

Base flow and case designation	Adjoint Solver	Disturbance energy, $\mathcal{E}_p$	Inflow $\sqrt{Re_{x_0}}$	Sensor $\sqrt{Re_{x_m}}$
Parallel (P)	ANS	-	2000	2000
Parallel (P-LST)	LST	-	2000	2000
Transitional (T)	ANS	$1.44 \times 10^{-5}$	1800	2000, 2350, 2650

Table 1. Flow configurations for computing the DOD using ANS or (LST. The base flow is either parallel or a spatially developing transitional boundary layer with initial disturbance energy  $\mathcal{E}_p$ . The inflow and measurement Reynolds numbers are reported.

Base flow and designation	Domain size $(L_x, L_y, L_z)$	Grid points $(N_x, N_y, N_z)$
Parallel (P)	(400, 200, 300)	(256, 150, 150)
Transitional (T)	(2553, 200, 250)	(1703, 150, 180)

Table 2. Domain sizes and grid numbers for solving the adjoint Navier–Stokes equations for different base flows, including parallel and transitional boundary layers.

gradually adjusted to the free-stream values within a distance of fifty spatial units. When we consider parallel boundary layers (cases P and P-LST in table 1), the Reynolds number is constant  $\sqrt{Re_{x_0}} = 2000$  and periodicity is enforced in the streamwise direction ( $x$ ). For the spatial boundary layer (case T in table 1), the inflow is prescribed as a superposition of a Blasius base state at  $\sqrt{Re_{x_0}} = 1800$  and instability waves. The lower Reynolds numbers at the inflow allow us to place a sensor at  $\sqrt{Re_{x_0}} = 2000$ , which can be compared with the parallel-flow configuration. The instability waves are Fourier modes in the spanwise direction, harmonic in time and their wall-normal profiles are eigenfunctions of the linear-stability operator. The modal amplitudes were optimised to achieve the earliest possible transition location when the total disturbance energy, here using Chu’s norm, is  $\mathcal{E}_p = 1.44 \times 10^{-5}$  (Jahanbakhshi & Zaki 2019). For each of the cases in table 1, the domains of dependence for wall-pressure sensors at  $\sqrt{Re_{x_m}}$  are computed either in physical space using the adjoint Navier–Stokes equations (ANS) or in spectral space using the linear-stability formulation (LST), according to the formulations in § 2.1 and § 2.2, respectively. The computational parameters are provided in table 2.

The example from the transitional case T is shown in figure 2. The grey contours represent the streamwise velocity, from DNS. The flow is initially laminar near the inflow ( $\sqrt{Re_{x_0}} = 1800$ ), is progressively more perturbed downstream and undergoes transition to turbulence near  $\sqrt{Re_x} = 2400$ . Superimposed on the forward field are colour contours of the adjoint density,  $\rho^\dagger$ , due to point measurement of wall pressure when the probe is placed within the turbulent flow at  $\sqrt{Re_{x_m}} = 2650$ . The four panels display  $\rho^\dagger$  at backward times  $\tau = t_m - t = \{100, 814, 1628, 2442\}$ . The DOD of the measurement, which is represented by the support of  $\rho^\dagger$ , starts from the adjoint impulse at the probe location and expands in backward time. At early backward time  $\tau = 100$ , the adjoint field is contained within the edge of the turbulent boundary layer, and breaches it by  $\tau = 814$  (figure 2b). The pattern of  $\rho^\dagger$  in the free stream resembles spherical wave fronts that propagates upstream. When the adjoint traverses from the turbulent to the laminar region in the boundary layer, it has an elongated streamwise appearance (figure 2c,d) and a more regular, harmonic pattern. In panel (d), at  $\tau = 2442$ , distinct waves with a larger wavelength compared with earlier

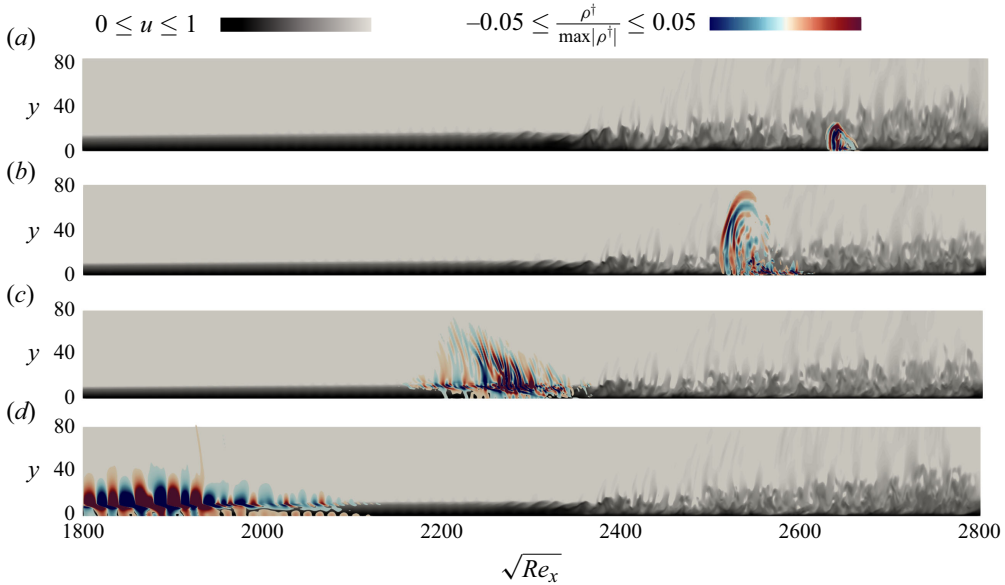


Figure 2. Streamwise velocity  $0 \leq u \leq 1$  (grey contours) and adjoint density  $-0.05 \leq \rho^\dagger / |\rho^\dagger|_{\max} \leq 0.05$  (colour contours) for case T, plotted at  $z = 0$  and (a-d)  $\tau = t_m - t = \{100, 814, 1628, 2442\}$ .

times are concentrated near the edge of the boundary layer. The trends identified in [figure 2](#) will be revisited once simpler configurations are examined in detail.

Just as the forward evolution of a disturbance in a boundary layer depends on whether the flow is laminar, transitional or turbulent, the evolution of the adjoint field from a sensor probe has distinct behaviours in these three regimes. It is therefore instructive to start from the laminar configuration, specifically, we will consider a probe placed within a temporal laminar boundary layer in [§ 3.1](#), and examine the connection to transient growth in [§ 3.2](#). We will then consider a spatial, transitional boundary layer in [§ 3.3](#), where we evaluate the impact of the sensor placement on the probe sensitivity, including when it is placed within the turbulent region similar to [figure 2](#).

### 3.1. Measurement domain of dependence in laminar boundary layer

We consider the parallel, laminar boundary layers at  $M = 4.5$  and  $\sqrt{Re_x} = 2000$ , with designations P and P-LST in [table 1](#). The former refers to solving the adjoint Navier–Stokes equation to study the DOD of a pressure measurement, while the latter is in reference to using the linear-stability operator (in spectral space) and its adjoint. For the adjoint Navier–Stokes solver, we employ periodic boundary conditions in the streamwise direction while freezing the base flow, which enables us to maintain consistency between the two approaches. The streamwise domain length was designed to ensure that the allowable wavelengths in the ANS simulations match those evaluated in the temporal LST. By examining a laminar case, we can compare and verify the adjoint Navier–Stokes and LST, and clearly identify properties of the wall-pressure sensor.

Iso-surfaces of the adjoint fields from case P are plotted in [figure 3](#), at different backward times,  $\tau = t_m - t$ . Each component of the adjoint state vector is normalised by its maximum value, and the boundary-layer edge is marked by a transparent plane located at  $y = \delta_{99} = 13.9$ . According to [\(2.16\)](#), the inner product between the adjoint

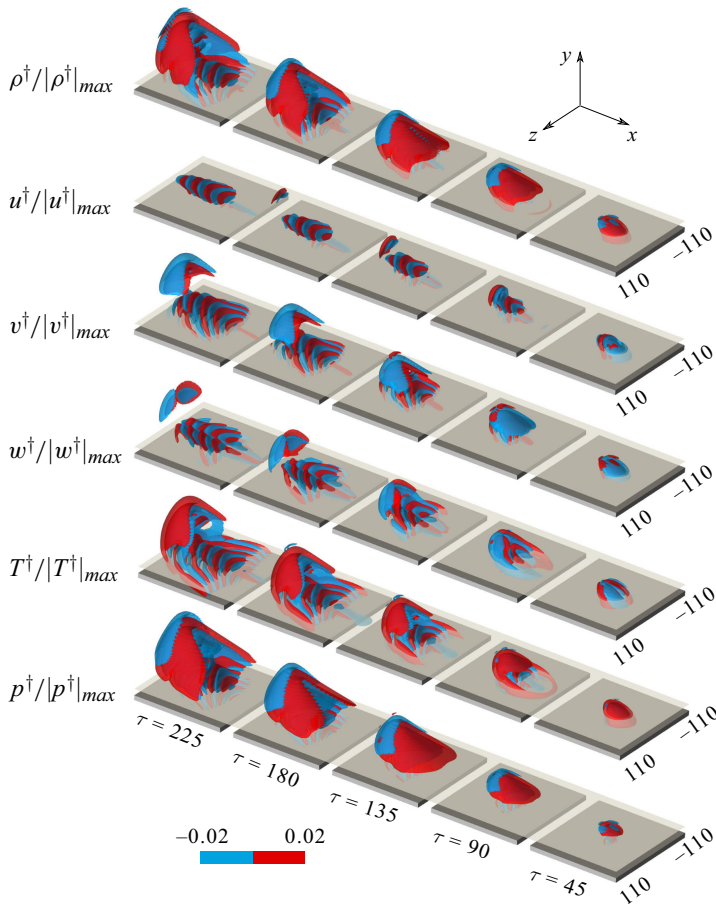


Figure 3. Adjoint fields starting from an impulse of pressure at the wall of a compressible temporal boundary layer. Iso-surfaces of different adjoint quantities are shown at backward time  $\tau = t_m - t = \{45, 90, 135, 180, 225\}$ .

field and a perturbation in the forward state represents the deviation in the measurement. Therefore, locations where the adjoint variables attain large magnitudes correspond to a high sensitivity of the measurement to fluctuations at these locations and in the corresponding flow component.

The adjoint originates from the wall as a pressure impulse, mathematically modelled as a two-dimensional Gaussian with standard deviation equals to four Blasius length scales. Changing the width of the Gaussian in the initial condition, for example decreasing it to two Blasius length scales, does not affect our findings and the resulting adjoint fields remain nearly identical. Since the sensor is at the wall, the local flow is subsonic. As such, in the early adjoint evolution, both upstream and downstream propagation of the adjoint field are possible. However, once the adjoint has crossed into the supersonic region of the boundary layer, and at the reverse times shown in [figure 3](#), the dominant structures are advected upstream. Furthermore, the upstream DOD splits into two regions: one is contained within the boundary layer and the other is a radiating acoustic wave outside the boundary layer, the latter representing the sensor sensitivity to incoming perturbations from the free stream. The alternating pattern of positive and negative values corresponds to

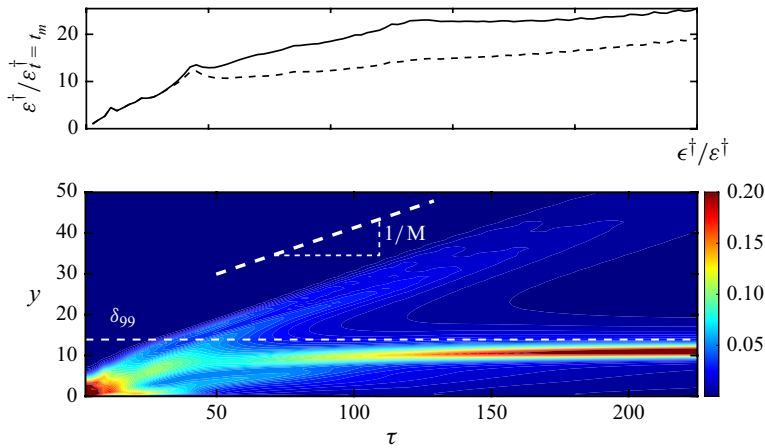


Figure 4. Energy distribution of adjoint field representing the sensitivity for pressure measurement. The top curves show the energy growth in the whole computational domain (solid line) and inside the boundary layer (dashed line), as a function of the backward time  $\tau$ , normalised by the initial energy of the adjoint  $\mathcal{E}^\dagger_{t=t_m}$ . The bottom contour shows the energy distribution along the vertical direction at different  $\tau$ . dashed white line marks the edge of the boundary layer,  $\delta_{99}$ .

a forward perturbation leading to an increase or decrease in the sensor measurement. Also interesting is the complement of this view: disturbances outside the support of the adjoint field in space–time are cloaked to the sensor. Perhaps more interestingly, even disturbances within the support of the adjoint field but orthogonal to it, i.e.  $\langle \mathbf{q}_0^\dagger, \delta \mathbf{q}_0 \rangle = 0$ , are cloaked to the sensor (see 2.18). The design of measurement campaigns can therefore attempt to capture these unobservable regions and disturbances by use of different sensor placements and modalities. As such, the DOD offers valuable insight for the design of effective sensor networks. In Appendix B, we provide an example where we contrast the forward evolutions of two initially localised, free-stream disturbances: an acoustic and an entropic one. The former is observable while the latter is entirely cloaked to the sensor. The example also serves as a validation of the accuracy of our implementation of the adjoint, by verifying the forward-adjoint duality relation.

A quantitative measure of the adjoint field is its energy

$$\mathcal{E}^\dagger = \int_y \epsilon^\dagger(y) dy = \int_y \frac{1}{2} \int_{x,z} \bar{\rho} \|\mathbf{u}^\dagger\|^2 + R \frac{\bar{T}}{\bar{\rho}} \rho^{\dagger 2} + \frac{R}{\gamma - 1} \frac{\bar{\rho}}{\bar{T}} T^{\dagger 2} dx dz dy, \quad (3.1)$$

where  $\epsilon^\dagger(y)$  is the energy integrated over the horizontal plane, and  $\mathcal{E}^\dagger$  is obtained by further integration in the wall-normal direction. The latter quantity can be integrated over the boundary-layer height only or the entire domain, in order to quantify the relative dependence of the sensor on boundary-layer versus free-stream disturbances, as shown in figure 4a. At early times, the boundary-layer portion (dashed line) is 100 % of the total energy (solid line). Beyond  $\tau \simeq 27$ , this fraction reduces to as little as 60 % at  $\tau = 135$ , and subsequently starts to recover at longer reverse times. Figure 4b shows  $\epsilon^\dagger(y)$  in backward time  $\tau$ , and provides a clear interpretation. While contours of  $\epsilon^\dagger$  are initially entirely contained within the boundary layer, a portion of the energy breaches  $\delta_{99}$  at  $\tau \simeq 27$  and propagates into the free stream as an adjoint acoustic wave (recall figure 3) that travels at the speed of sound, as marked in the figure. The part of  $\epsilon^\dagger$  that remains within the boundary layer amplifies exponentially at large  $\tau$ . The highest adjoint energy is recorded below  $\delta_{99}$ , around  $y = 10$ , which we will later relate to a critical layer at that

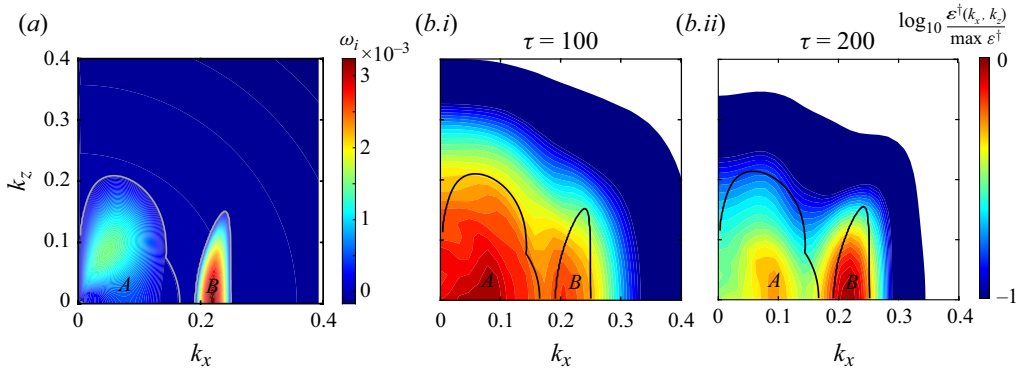


Figure 5. (a) Contours of eigenvalues for the most unstable/least stable modes at different  $(k_x, k_z)$ . The neutral curve is plotted with the grey line in the background. (b) Contours of the logarithmic of the normalised energy in the adjoint fields at different  $(k_x, k_z)$  and different backward times  $\tau = \{100, 200\}$ . The neutral curve is plotted in the black line as a reference.

position. The expansion and amplification of the DOD in backward time imply that a larger region becomes observable and that the measurement is more sensitive to events farther away from the probe position. To understand the latter effect, consider a fixed initial perturbation energy: If the perturbation is close to the sensor, it may have an immediate impact on the measurement, while perturbations farther upstream can grow through modal and non-modal mechanisms prior to reaching the probe.

The late-time amplification of  $\epsilon^\dagger$  near the boundary-layer edge coincides with the wave-like patterns near  $\delta_{99}$  in figure 3, which are most evident in  $(u^\dagger, v^\dagger, w^\dagger)$  at  $\tau = \{180, 225\}$ . This observation motivates a spectral decomposition of the adjoint fields. To anchor the discussion to established knowledge, we first report results from linear-stability analysis of the temporal boundary layer. At every wavenumber pair  $(k_x, k_z)$ , we solve the eigenvalue problem and identify the most unstable mode. Contours of the modal growth rate are reported in figure 5(a), where two distinct regions of instability are marked A and B, and identified by their respective neutral curves. These regions correspond to the familiar first and second Mack modes (Mack 1984).

The energy-spectral density of the adjoint field is plotted in figure 5(b), as a function of the horizontal wavenumbers. Superimposed on the contours are the neutral curves (black lines) from the forward linear-stability analysis, reproduced from figure 5(a). Since the adjoint field is initialised at  $\tau = 0$  as a Gaussian kernel in the homogeneous directions, the initial energy distribution is also a Gaussian centred around the origin. As the adjoint field evolves in backward time, distinct growth rates come into play. At  $\tau = 100$ , the energy distribution is still concentrated in the low-wavenumber region. However, it is modified by amplification at wavenumber  $(k_x, k_z) = (0.1, 0)$  which coincides with the first mode from the forward problem, and by a secondary peak at  $(k_x, k_z) = (0.22, 0)$  within the Mack second-mode region. At larger backward times,  $\tau = 200$ , the peak around  $(k_x, k_z) = (0.22, 0)$  becomes dominant. This description should not be misinterpreted as a banal restatement of the forward modal instability. Equation (2.27) expressed the adjoint in terms of the forward modes. One can therefore expect that the most unstable wavenumbers of the forward dynamics dominate at long times. In the context of the sensor DOD, those modes will amplify the most during the forward evolution, and may lead to a significant signature at the sensor. Whether this behaviour materialises in the adjoint is not a foregone conclusion, and depends on the observation operator which appears in (2.27). In the case

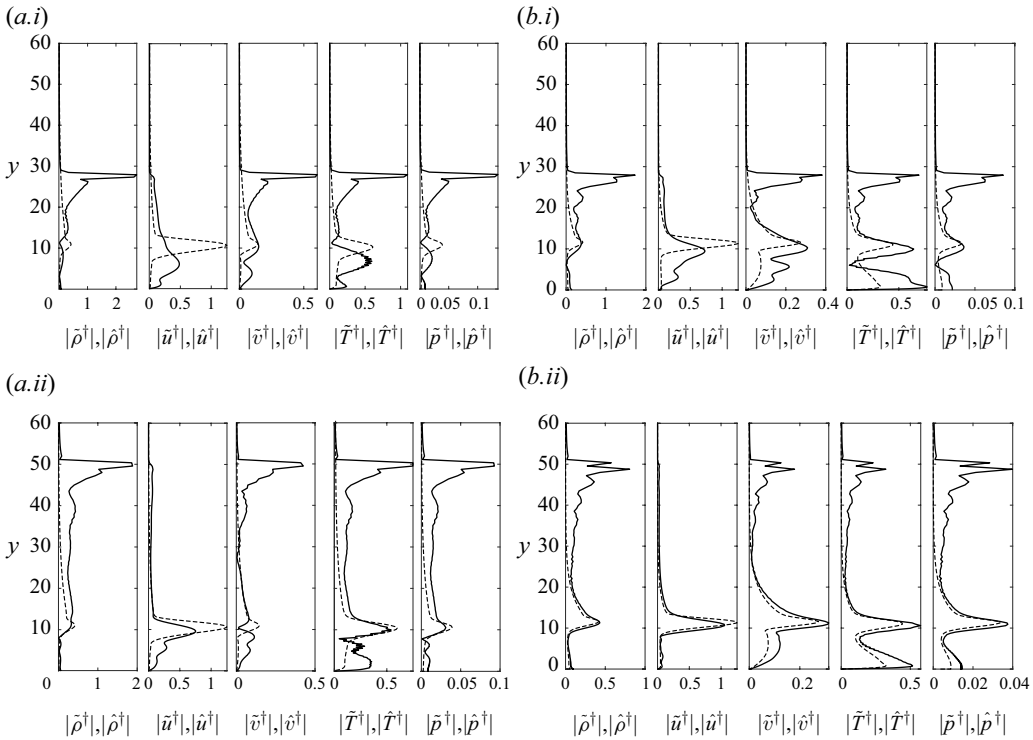


Figure 6. (a) Solid black lines represent the mode shape of the adjoint fields for the wavenumber pair  $(k_x, k_z) = (0.1, 0)$  (region A) at backward times (a.i)  $\tau = t_m - t = 100$  and (a.ii)  $\tau = 200$ , starting from a pressure measurement at the wall evaluated using LST with transient growth formulation. Shapes of the most unstable adjoint mode at the same wavenumber pair in these components are shown in dashed lines. (b) Similar to (a), but the wavenumber pair is  $(k_x, k_z) = (0.2, 0)$  (region B).

of a wall-pressure sensor, the wall signature of the forward most unstable modes is indeed sufficient to dominate the sensor sensitivity at long times. In other words, measurements from wall-pressure sensors in the laminar region of the flow can be accurately assimilated to predict the upstream second-mode waves, although one should caution that a material fraction of the sensor signal may be due to incident free-stream waves (see figure 4).

The profiles of the adjoint fields at the peak wavenumbers in regions A and B are reported in figures 6(a) and 6(b), at two times  $\tau = \{100, 200\}$  (top and bottom panels). These results for sensor DOD were computed using (2.27), namely the transient-growth formulation, and the profiles are normalised to unit modal energy under Chu’s norm.

The dashed lines in the figures are profiles of the most unstable eigenfunction of the adjoint LST operator, and are included for comparison.

At both times  $\tau = t_m - t = \{100, 200\}$ , all components of the sensor DOD (solid curves) have an appreciable portion in the free stream, except  $\hat{u}$ . As such, a streamwise-velocity perturbation from the free stream is ineffective at creating a pressure signature at the sensor position at  $t_m$ . In all cases, the perturbations in the free stream satisfy the dimensionless relations for an isentropic acoustic wave (Kovasznay 1953)

$$|\hat{\rho}^\dagger| = M^2 |\hat{p}^\dagger|, \quad |\hat{T}^\dagger| = (\gamma M^2 - 1) |\hat{p}^\dagger|, \quad |\hat{v}^\dagger| = M |\hat{p}^\dagger|. \quad (3.2)$$

At the larger backward time, the free-stream portion has propagated farther from the boundary-layer edge at the free-stream speed of sound,  $\Delta y = \Delta \tau / M = 100 / 4.5 \approx 22.2$ .

Within the boundary layer, the DOD profiles have high values around the critical layer ( $y = 10$ ), which agrees with the overall energy distribution in [figure 4](#). In other words, the wall-pressure sensor has high sensitivity to perturbations in this region, especially when they can amplify for sufficient time prior to reaching the sensor. In addition, the profiles exhibit a growing resemblance to the most unstable eigenfunction of the adjoint linear-stability operator. This tendency is particularly pronounced for mode  $(k_x, k_z) = (0.22, 0)$ , within region *B*. Evolving the adjoint field for an extended temporal duration is essentially the outcome of repeatedly multiplying it by the adjoint operator, thus progressively aligning it with the principal adjoint eigenfunctions. The rate of convergence to the principal adjoint eigenfunction depends on the separation in growth rates between the least stable modes. Therefore, we observe a considerably faster convergence of the Fourier components of the adjoint field within region *B*, relative to *A*. In addition, while one may have intuitively expected that the sensor would be most sensitive to the most unstable forward mode, the reality is different. The sensitivity of the pressure measurement at the wall is most pronounced along the direction set by the adjoint eigenfunction, which is a composite of various forward eigenmodes. In reverse time, this adjoint eigenfunction propagates upstream as an instability wave, with most of its energy concentrated near the boundary-layer edge. The impact of free-stream acoustic waves also contributes to the sensor sensitivity. These two effects combine optimally, depending on the measurement time, to influence the sensor measurement.

### 3.2. Forward evolution of the sensor DOD in laminar boundary layer

In [§ 2.2](#), the measurement DOD was interpreted in the context of transient growth. The adjoint field at  $\tau = t - t_m$  is the optimal perturbation with unit energy that, in the forward evolution, maximises the norm of the sensor measurement at  $t = t_m$ . We examine this property by prescribing the initial forward perturbation  $\delta \hat{\mathbf{q}}_0 = \hat{\mathbf{q}}_0^\dagger$ , and computing its forward evolution.

As an example, we consider the DOD at  $(k_x, k_z) = (0.1, 0)$ , when the measurement is the wall pressure at  $t_m = 200$ . This adjoint field is adopted as an initial disturbance, and [figure 7](#) examines its forward evolution. [Figure 7\(a\)](#) shows side views of the pressure field at forward time instances  $t = \{0, 100, 200, 300, 400\}$ , with the corresponding wall-normal profiles plotted in [figure 7\(b\)](#). The initial disturbance ( $t = 0$ ), which is also the adjoint profile, clearly comprises two parts: the free-stream acoustic wave and the boundary-layer component. During the forward evolution, the acoustic wave propagates towards the wall, traverses the boundary-layer edge, and interacts with the boundary-layer portion. The outcome maximises the measurement at time  $t = t_m = 200$ , resulting in the largest possible norm of the wall-pressure signature. The evolution of the wall-pressure magnitude is reported in panel (c). As anticipated, the curve peaks at  $t = t_m = 200$ . This result helps tie the notion of the sensor DOD, or sensitivity, to the disturbance that maximises the measurement. The complement to this point of view is also worth reiterating: disturbances that are orthogonal to the adjoint field have zero impact on the measurement (for an example, see [Appendix B](#)).

When examining the forward evolution of  $\delta \hat{\mathbf{q}}_0 = \hat{\mathbf{q}}_0^\dagger$ , it is perhaps most instructive to express the perturbation field in terms of eigenmodes of the forward operator,  $\hat{\mathbf{q}}_0^\dagger = \sum_j b_j \tilde{\mathbf{q}}_j$ . The coefficients  $b_j$  are obtained with the aid of the bi-orthogonality relation

$$\langle \tilde{\mathbf{q}}_i, \tilde{\mathbf{q}}_j^\dagger \rangle = \sigma_j \delta_{ij}, \tag{3.3}$$

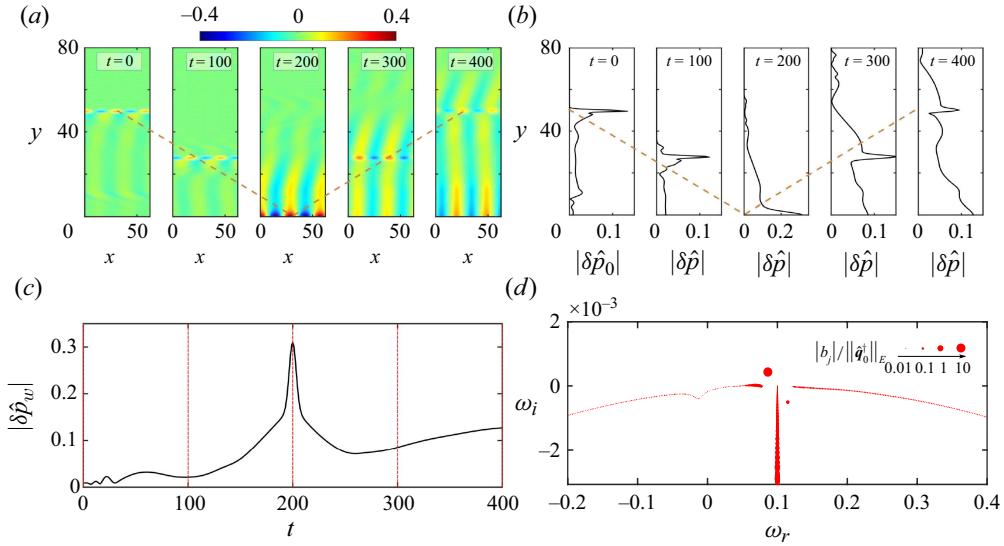


Figure 7. Forward evolution of the pressure field from an initial disturbance  $\delta \hat{\mathbf{q}}_0 = \hat{\mathbf{q}}_0^\dagger$ , at  $(k_x, k_z) = (0.1, 0)$  (region A). (a) Contours of  $\delta p$  in physical space and (b) wall-normal profiles of  $\delta \hat{p}$ , at selected time instances  $t = \{0, 100, 200, 300, 400\}$ . (c) The wall-pressure signature as a function of time. Dashed lines mark the time instances reported in panels (a,b). (d) Decomposition of the adjoint fields onto the forward eigen-basis. Larger symbols represent larger coefficient  $|b_j|/||\hat{\mathbf{q}}_0^\dagger||_E$  of adjoint fields projected onto the forward eigenbasis, calculated using the expression (2.26).

where  $\delta_{ij}$  is the Kronecker delta. Using the expansion of the adjoint field and bi-orthogonality, we can write

$$\langle \hat{\mathbf{q}}_0^\dagger, \tilde{\mathbf{q}}_j^\dagger \rangle = \sum_i b_i \langle \tilde{\mathbf{q}}_i, \tilde{\mathbf{q}}_j^\dagger \rangle = \sigma_j b_j, \quad b_j = \frac{\langle \hat{\mathbf{q}}_0^\dagger, \tilde{\mathbf{q}}_j^\dagger \rangle}{\langle \tilde{\mathbf{q}}_j, \tilde{\mathbf{q}}_j^\dagger \rangle} = \frac{\langle \hat{\mathbf{q}}_0^\dagger, \tilde{\mathbf{q}}_j^\dagger \rangle}{\sigma_j}. \quad (3.4)$$

The above projection (3.4) of the sensor DOD onto the forward eigenfunction basis yields the same result as (2.26), namely  $\mathbf{b} = \mathbf{G}^{-1}(\mathbf{A}^{t_m})^H \mathbf{O}^H$ ; we used this equivalence for numerical verification.

Figure 7(d) provides a representation of the projection coefficients,  $b_j$ . Each point in the figure marks an eigenvalue of the forward temporal-stability operator, at  $(k_x, k_z) = (0.1, 0)$ . The sizes of the points represent the magnitudes  $|b_j|/||\hat{\mathbf{q}}_0^\dagger||_E$  in logarithmic scale, where the normalisation uses the energy norm of the adjoint field at the initial time. The largest contribution from a single mode is by the slow acoustic wave, which has the largest  $|b_j|$ . Since the slow mode features prominently in the adjoint sensitivity, it is expected to contribute appreciably to the measurement in a forward evolution. However, this figure also underscores that the sensitivity is not a single forward mode in isolation, but rather a superposition of all the shown modes that, together, yields the largest possible outcome at the measurement. For example, modes along the fast acoustic and slow acoustic continuous branches individually make a modest contribution to the adjoint sensitivity, as reflected by their relatively small  $|b_j|$ . However, they are essential in the expansion. This fact may be inferred from figure 7(a,b): the second-mode wave does not, for example, account for the free-stream sensitivity which, as we demonstrate below, makes an appreciable contribution to the sensor signal.

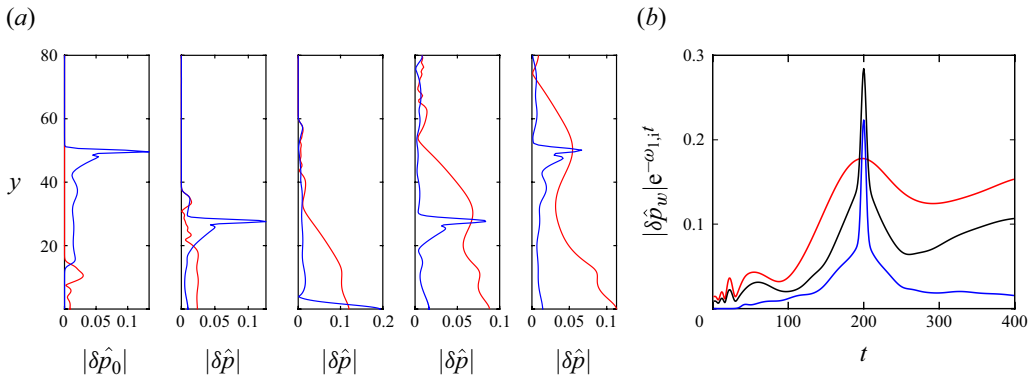


Figure 8. (a) The forward evolution of a disturbance equal to the adjoint field from a wall-pressure measurement at time  $t_m = 200$  and wavenumbers  $(k_x, k_z) = (0.1, 0)$ . The disturbance is decomposed into the near-wall (red lines) and outer acoustic (blue lines) parts, and is reported at times  $t = \{0, 100, 200, 300, 400\}$ , normalised to unit initial energy. Panel (b) shows the wall-pressure measurements from the near wall, outer acoustic and the combined disturbance. All profiles are normalised by  $e^{\omega_{1,i}t}$ .

We decompose the adjoint DOD into two parts: the boundary-layer portion and the outer acoustic wave. This step is achieved by multiplying  $\delta\hat{q}_0 = \hat{q}_0^\dagger$  by a hyperbolic tangent function that approximates a Heaviside function at the edge of the boundary layer,  $y = 13.9$ . This decomposition is motivated by the shape of the full adjoint field at large reverse time, rather than its eigen-representation which would require special attention to the treatment of the continuous modes that may bridge the free stream and the boundary layer. The forward evolution of the inner and outer parts of the profile, each normalised to unit initial energy, is shown in figure 8(a) (red and blue curves). The associated wall-pressure signatures are reported in panel (b). The wall-pressure signatures are normalised by the amplification of the most unstable forward mode,  $e^{\omega_{1,i}t}$ . A few observations are noteworthy: (i) the wall-pressure signature of the boundary-layer portion is smooth, while the signature of the free-stream portion is more localised around  $t = t_m$ . This qualitative difference facilitates distinguishing the two contributions. (ii) The time-dependent boundary-layer portion is not exponential. As such, this part of the profile is not solely a second-mode instability, but rather a superposition of waves that are subject to transient amplification. For reference, purely modal amplification would appear as a horizontal line on this graph, since the pressure signal is normalised by the maximum possible modal growth rate. (iii) It is apparent that placing all the  $\hat{q}_0$  in either the boundary-layer portion or in the free-stream acoustic wave alone will not achieve the highest possible wall signature at the target measurement time,  $t = t_m = 200$ . (iv) Instead, the total adjoint field  $\hat{q}_0^\dagger$  captures the optimal proportionality of the two parts, which achieves the maximum, appreciably larger, wall-pressure signature. The ratio of the energy in the two components, similar to the results in figure 4, is approximately 70% in the boundary layer and 30% in the free stream.

The results in figure 9 are at wavenumbers  $(k_x, k_z) = (0.22, 0)$ . The forward evolution of the inner and outer parts of the profile, each normalised to unit initial energy, is shown in figure 9(a) in red and blue curves, respectively. The time evolution of the wall pressure is plotted in panel (b), normalised by  $e^{\omega_{1,i}t}$ . Compared with the case with wavenumbers  $(k_x, k_z) = (0.1, 0)$ , the contribution from the boundary-layer portion of the adjoint profile accounts for the majority of the wall-pressure signature. At long times, the normalised

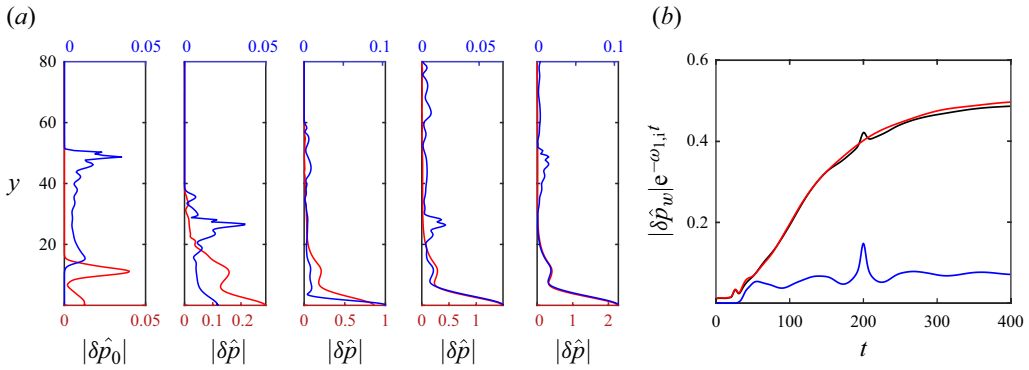


Figure 9. (a) The forward evolution of a disturbance equal to the adjoint field from a wall-pressure measurement at time  $t_m = 200$  and wavenumbers  $(k_x, k_z) = (0.22, 0)$ . The disturbance is decomposed into the near-wall (red lines) and outer acoustic (blue lines) parts, and is reported at times  $t = \{0, 100, 200, 300, 400\}$ , normalised to unit initial energy. Panel (b) shows the wall-pressure measurements from the near wall, outer acoustic, and the combined disturbance. All profiles are normalised by  $e^{\omega_{1,i}t}$ .

wall pressure is nearly constant, which indicates that the forward evolution of the adjoint from large  $t_m$  aligns with the exponential amplification of the second mode.

The results in this section supplement the interpretation of the DOD of a wall-pressure sensor in laminar flow, by computing the forward evolution of the DOD field. The free-stream and boundary-layer portions of the DOD were distinguished in order to stress their respective contributions and the outcome of their superposition. While the superposition has the largest impact on the sensor signal at the measurement time, the relative importance of the two parts depends on the wavenumber of the disturbance. This information can be particularly important when interpreting wall-pressure measurements in noisy free-stream conditions.

### 3.3. Measurement domain of dependence in transitional boundary layer

We now return to the more complex case of a spatially developing, transitional boundary layer. As noted earlier, the DOD of wall-pressure measurement within the preceding flow state is a function of the sensor placement, whether it is located in the laminar, transitional or fully turbulent region of the flow. A spatially developing, transitional boundary layer enables comparison of these three regimes (cases T in table 1). A sample flow field from case T is shown in figure 10, where the sensor is positioned at  $\sqrt{Re_{x_m}} = 2350$ , within the transitional zone, or upstream of the fully turbulent boundary layer. The grey contours show the forward streamwise velocity at two back-in-time instances relative to the measurement, at  $\tau \equiv t_m - t = 450$  and 1600. The colour contours show the DOD of the sensor, in terms of the adjoint density. Similar qualitative characteristics to the temporal case are evident in the figure: a free-stream component appears as wave fronts travelling at the Mach angle and a boundary-layer component elongates and amplifies in backward time. Properties of the adjoint field will be evaluated and compared for different positions of the measurement probes, and we will comment on the implication in the context of the interpretation of the measurements in data assimilation.

For case T, we consider three probe locations within the laminar, transitional and turbulent regions of the flow, at  $\sqrt{Re_{x_m}} = \{2000, 2350, 2650\}$ . The first position was selected to match the Reynolds number of the temporal boundary layer that we discussed previously, at  $\sqrt{Re_x} = 2000$ . This case then serves as a reference for comparison with

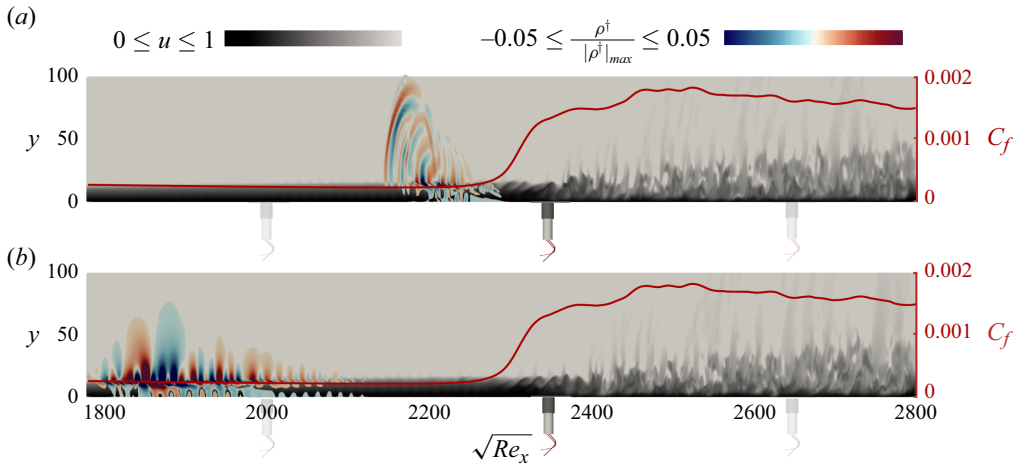


Figure 10. Grey contours of streamwise velocity for case T, overlaid by colour contours of the adjoint density from a wall-pressure probe at  $\sqrt{Re_{x_m}} = 2350$ . The two instances correspond to (a)  $\tau = 450$  and (b)  $\tau = 1600$ . Two other sensor locations,  $\sqrt{Re_{x_m}} = \{2000, 2650\}$  are marked by transparent probes on the figures. The mean skin-friction coefficient curve  $C_f$  is plotted to further distinguish the laminar, transitional and turbulent regions.

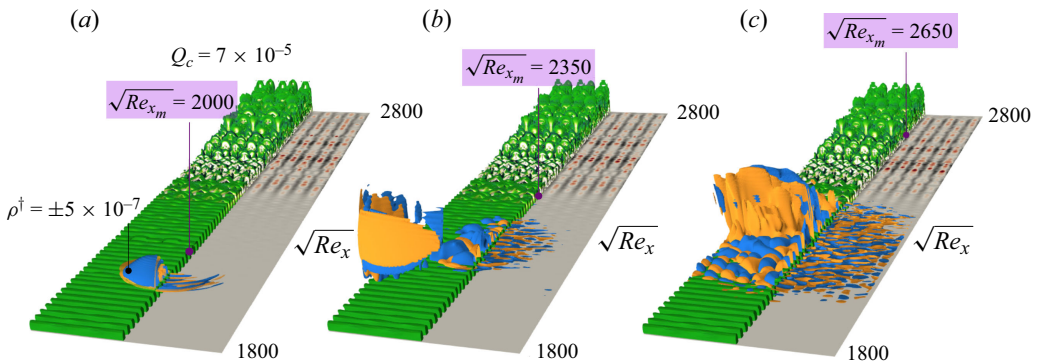


Figure 11. Iso-surface of the streamwise velocity  $u = 0.9U_\infty$ , coloured by the fluctuation velocity  $u'$ . The left half of each panel shows the coloured contour of the skin-friction fluctuation,  $c'_f = \mu / Re \partial u' / \partial y / (1/2 \rho_\infty U_\infty^2)$  between  $-0.001$  and  $0.001$ . The iso-surfaces in the laminar region show the normalised adjoint density  $\rho^\dagger / \max |\rho^\dagger|$  from a wall-pressure sensor in the (a) laminar  $\sqrt{Re_{x_m}} = 2000$  (b) transitional  $\sqrt{Re_{x_m}} = 2350$  and (c) turbulent  $\sqrt{Re_{x_m}} = 2650$  regions. The backward time is chosen such that the adjoint has reached similar upstream position. The iso-surfaces are divided by the edge of the boundary layer into the outer parts, shown on the left, and the inner part of the boundary layer, shown on the right.

the other probes. Three-dimensional views of the forward and adjoint fields are shown in figure 11. The former are visualised by iso-surfaces of the  $Q$  criterion and contours of the skin-friction coefficient at the wall. The positions of the wall-pressure probes are marked in the figures, and the associated adjoint fields,  $\rho^\dagger / \max |\rho^\dagger|$ , are visualised when they reach nearly the same upstream location in order to compare their sensitivities with events that take place near the inflow. The visualisation is dissected in the span in order to contrast the free-stream and boundary-layer portions of the sensor DOD. The wave-front appearance of the former and the wave-train shape of the latter are evident for the upstream

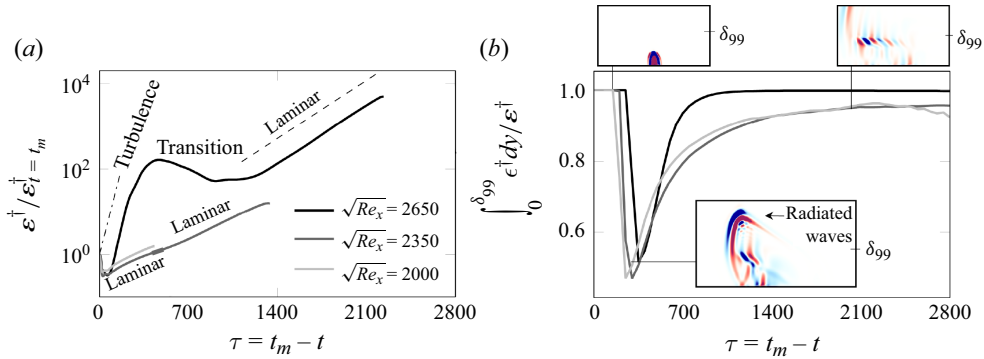


Figure 12. (a) Energy amplification versus backward time  $\tau = t_m - t$  for case  $T_1$  and the three sensor placements. Darker colours represent probes at larger downstream distances,  $\sqrt{Re_{x_m}} = \{2000, 2350, 2650\}$ . (b) Ratio of adjoint energy inside the boundary layer to the total energy versus backward time.

most sensor. The wave train within the boundary layer is structured, spreads and amplifies in backward time, and has a dominant streamwise wavenumber. These characteristics are most evident in the adjoint field from the most upstream sensor and, while discernible from the last one, are distorted by the adjoint field having traversed the turbulent and turbulent-to-laminar regions. The adjoint in this case, starting from a sensor at  $\sqrt{Re_{x_m}} = 2650$ , is larger in text and its magnitude is at least more than two orders of magnitude larger than the other cases. In addition, the visualised iso-surfaces above the boundary layer are not the dependence on an incoming free-stream acoustic wave that is directly incident onto the sensor, as discussed in the temporal problem and observed for the two upstream sensors. For the third sensor placement, that part of the adjoint field has already propagated beyond the visualised volume at the reported time,  $\tau = 1800$ . The observed protrusion of the DOD beyond the edge of the boundary layer is a continued sensitivity to edge disturbances that can interact with the boundary layer and lead to a modification of the sensor signal post transition. The connection between the characteristics of these adjoint fields and data assimilation, or more specifically the cost function of the data-assimilation problem, is noteworthy. The adjoint field that emanates from the turbulent region is qualitatively less structured, or more chaotic in nature, which mirrors a typical feature of the gradient of cost functions with observations within a turbulent field. These cost functions often exhibit non-convexity, with large local gradients and extreme curvatures, making the optimisation process more intricate due to the presence of multiple local minima.

A quantitative comparison of the adjoint fields from the three sensor locations is reported in figure 12(a), where the adjoint energy is plotted as a function of backward time. For sensors in the laminar region, sensitivity amplifies exponentially and agrees with the growth rate for the most unstable mode from linear theory. When the sensor is within the turbulent region, the adjoint amplification is initially at a much steeper rate. As the adjoint traverses the turbulence-to-laminar region during its back-in-time upstream propagation, its energy decays slightly, followed by the exponential amplification within the laminar regime. The fraction of the adjoint energy that is contained within the boundary layer is plotted in figure 12(b). For all three sensors, the fraction that propagates into the free stream is up to approximately 45%, which indicates that in the forward problem incident Mach waves from the free stream can have an equal influence on the wall-pressure signal as a boundary-layer disturbance.

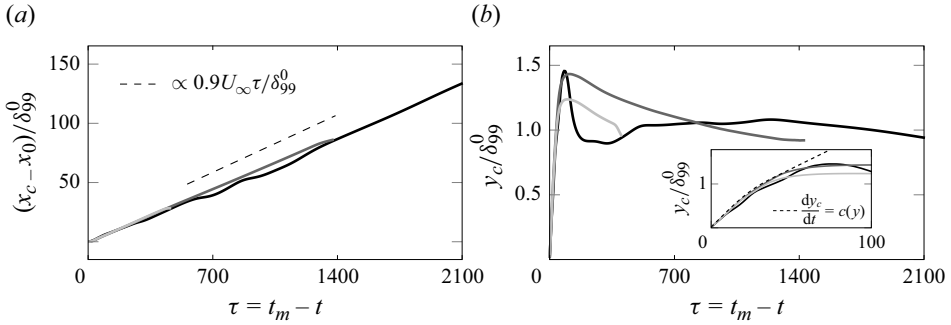


Figure 13. (a) Streamwise  $x_c$  and (b) wall-normal  $y_c$  positions of the centroid, evaluated according to (3.5). Darker solid lines correspond to sensors further downstream,  $\sqrt{Re_{x_m}} = \{2000, 2350, 2650\}$ . The dotted line in (b) marks the vertical position assuming the adjoint travels at the local speed of sound.

To further characterise the adjoint fields, we compute their centroids

$$\mathbf{x}_c = \frac{\int_{\mathcal{V}} \mathbf{x} \mathbf{q}^\dagger \mathbf{T} \mathbf{E} \mathbf{q}^\dagger d\mathcal{V}}{\int_{\mathcal{V}} \mathbf{q}^\dagger \mathbf{T} \mathbf{E} \mathbf{q}^\dagger d\mathcal{V}}, \tag{3.5}$$

and the tensor of moments

$$\mathcal{I} = \frac{\int_{\mathcal{V}} (\mathbf{x} - \mathbf{x}_c) (\mathbf{x} - \mathbf{x}_c)^\mathbf{T} \mathbf{q}^\dagger \mathbf{T} \mathbf{E} \mathbf{q}^\dagger d\mathcal{V}}{\int_{\mathcal{V}} \mathbf{q}^\dagger \mathbf{T} \mathbf{E} \mathbf{q}^\dagger d\mathcal{V}}. \tag{3.6}$$

We will evaluate these properties in two dimensions, specifically the streamwise-vertical coordinates, e.g.

$$\mathcal{I} = \begin{bmatrix} I_{xx} & I_{xy} \\ I_{xy} & I_{yy} \end{bmatrix} \tag{3.7}$$

which has two principal directions with associated stretches  $\lambda_\pm$  and angle  $\theta$ , given by

$$\lambda_\pm = \frac{1}{2} \left( I_{xx} + I_{yy} \pm \sqrt{(I_{xx} - I_{yy})^2 + 4I_{xy}^2} \right), \quad \theta = \frac{1}{2} \tan^{-1} \left( \frac{2I_{xy}}{I_{xx} - I_{yy}} \right). \tag{3.8}$$

The centroid locations  $(x_c, y_c)$  of the adjoint fields are reported in figure 13. In panel (a), the upstream advection within the boundary layer is captured by the change in  $x_c$  as a function of  $\tau$ , which yields an indication that the advection speed is approximately equal to 90 % of  $U_\infty$ . The evolution of  $y_c$  in figure 13(b) indicates that the adjoint field, once initialised at the sensor position, swiftly moves towards the boundary-layer edge at approximately the local speed of sound (see inset).

The expansion of the DOD of the last sensor is examined in figure 14, which also shows the skin-friction coefficient to distinguish the turbulent, transitional and laminar regions. The solid curves show the energy of the adjoint, integrated in the cross-flow plane, at  $\tau = \{0, 22.5, 117, 261, 805\}$ . Throughout the evolution, the predominant stretching of the adjoint field is in the streamwise ( $x$ ) direction, as the angle  $\theta \leq 0.1$  decreases with  $\tau$ . Given the alignment of the adjoint field with the streamwise direction, we mark on the figure  $x_c \pm \lambda_+$ . In both turbulent and transitional regions, the adjoint energy is contained within a compact streamwise extent, and is oscillatory which is indicative of a pronounced inhomogeneity. The exact pattern of the oscillation would necessarily vary depending on the time of release since it is dependent on the state of the forward turbulent flow; this

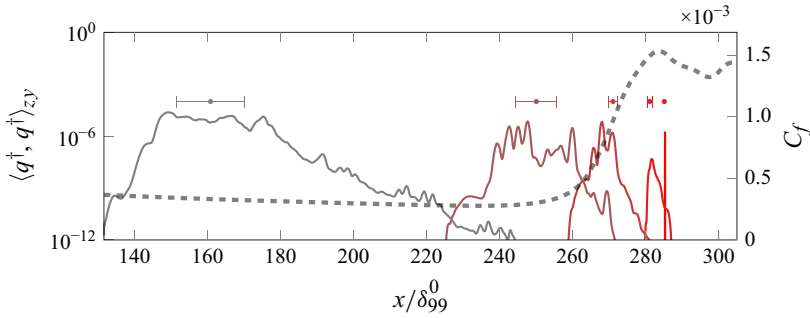


Figure 14. Streamwise distribution of the  $zy$  integrated adjoint profile, for  $\sqrt{Re_{x_m}} = 2650$ . Filled circles mark the streamwise coordinate of the centroid,  $x_c$ , and  $| \text{---} |$  is  $2\lambda_+$ . Red to grey solid curves represent  $\tau = \{0, 22.5, 117, 261, 805\}$ . The dashed line is the skin-friction coefficient,  $C_f = \mu/Re\partial U/\partial y/(1/2\rho_\infty U_\infty^2)$ , included to highlight stretching of the adjoint across transition.

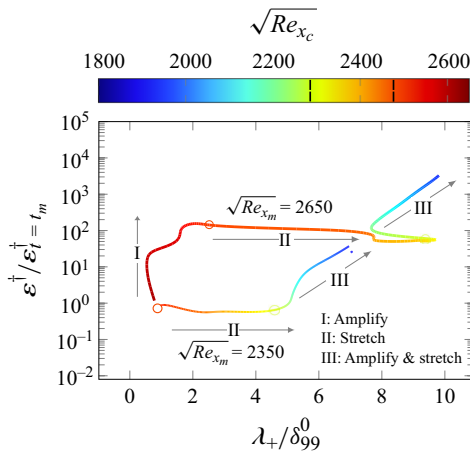


Figure 15. Dependence of sensitivity amplification and size of the adjoint structure along major  $x$  axis. Colour indicates increasing  $x_c$  in the  $\sqrt{Re_x}$  coordinate. On each curve, two circles mark the Reynolds numbers at the end and start of the transition zone.

dependence thus points to the difficulty of interpreting wall-pressure measurements within the turbulent region. Within the laminar region, the spreading of the DOD is evident, and leads to a smoothly distributed sensitivity over a longer extent. The wall-pressure sensor can therefore observe disturbances within this upstream region with nearly uniform sensitivity.

The evolution of the size and energy of the DOD are co-examined in figure 15. Each point on this stretching-amplification map corresponds to the sensor DOD at an instance in backward time, starting from two different sensor locations,  $\sqrt{Re_{x_m}} = \{2350, 2650\}$ . The curves start when the initial concentrated adjoint pulse from the sensor location is locally diffused a few grid points. The line colour corresponds to the Reynolds number based on the centroid position  $\sqrt{Re_{x_c}} = \sqrt{x_c Re}$ . Upstream advection is represented by the change in the colour from red to blue, and the two circles on each curve mark the end and start of transition to turbulence. The back-in-time evolution of the DOD exhibits three general behaviours: (I) energy amplification, (II) stretching and (III) simultaneous stretching and amplification.

Considering the sensor in the turbulent region,  $\sqrt{Re_{x_m}} = 2650$ , all three behaviours are observed starting with (I) energy amplification without appreciable stretching of the adjoint field. During this part of the evolution, the adjoint energy intensifies by two orders of magnitude. This early stage is best understood by considering the anticipated change in the spectral content of the adjoint. Since the turbulent forward field appears in the adjoint equation, the early evolution will feature amplification of the adjoint energy across a wide range of wavenumbers, while the spatial extent is localised. As the adjoint field traverses the turbulent-to-laminar transition region, it experiences significant stretching without energy amplification. This behaviour (II) is also observed when the sensor is placed at  $\sqrt{Re_{x_m}} = 2350$  and hence the start of the adjoint evolution is immediately at the onset of this back-in-time base-flow ‘laminarisation’ process. The stretching in physical space can be due to the decay of the small scales within the adjoint field, akin to the increase of the integral length scale as a function of time in decaying isotropic turbulence. The simultaneous stretching and amplification (III) is observed for both curves, within the laminar-flow regime, and is congruent with the results for the parallel boundary layer (§ 3.1). The adjoint field amplifies according to the behaviour of its constituent modes from LST. The dispersive nature of these modes leads to spreading in physical space, and the dominance of particular wavenumbers leads to energy amplification and an expected localisation of the peak energy in spectral space.

In summary, the intense amplification in (I) signals turbulence and chaotic dynamics, the stretching in (II) marks an expansion of the DOD across back-in-time laminarisation. The simultaneous amplification and stretch in (III) are symptomatic of the exponential growth rate captured by linear theory in the laminar regime.

These characteristics of the sensor DOD have implications for the assimilation of wall-pressure measurements in compressible, transitional boundary layers. When solving this inverse problem, two key challenges come to the forefront: (i) disturbances amplify exponentially both in forward and in backward time. The amplification in forward time is more familiar, and implies that small errors in the estimated initial and boundary conditions can lead to appreciable deviations of the assimilated state from the observations. In backward time, discrepancies from available measurements will amplify exponentially during the adjoint evolution and hence late measurements dominate the update of the estimated state. (ii) The second challenge is related to the landscape of cost function. According to (2.15), the Hessian is related to this amplifying adjoint field. As such, the cost landscape develops very large local curvatures and becomes more difficult to navigate for longer assimilation horizon. This difficulty is naturally most severe when the sensors are embedded in the turbulent region and hence the cost landscape is tortuous.

Spectral analysis of the adjoint fields enables us to examine how different frequencies and wavenumbers within the flow may contribute to the measurement, and enables us to relate our finding to the body of knowledge from linear stability of boundary layers. At the inflow, the boundary layer is laminar, and the Reynolds number is  $\sqrt{Re_x} = 1800$ . A forward spatial stability analysis of the Blasius flow at this Reynolds number was performed. For a range of  $(F, \beta)$ , the maximum growth rate,  $\alpha_i$ , was computed and is plotted in figure 16(a), where the neutral curve is also marked. The neutral curves at two additional positions,  $\sqrt{Re_x} = \{2000, 2350\}$  (location of the first two sensors), were also evaluated and all three curves are marked in figure 16(b). The colour contours in those figures are the normalised energy spectra of the adjoint field released from the three sensor positions,  $\sqrt{Re_{x_m}} = \{2000, 2350, 2650\}$ , and collected at the inflow.

For the sensor located at  $\sqrt{Re_x} = 2000$ , upstream of transition, the amplification of the adjoint field takes place largely within the range of frequencies and spanwise wavenumbers

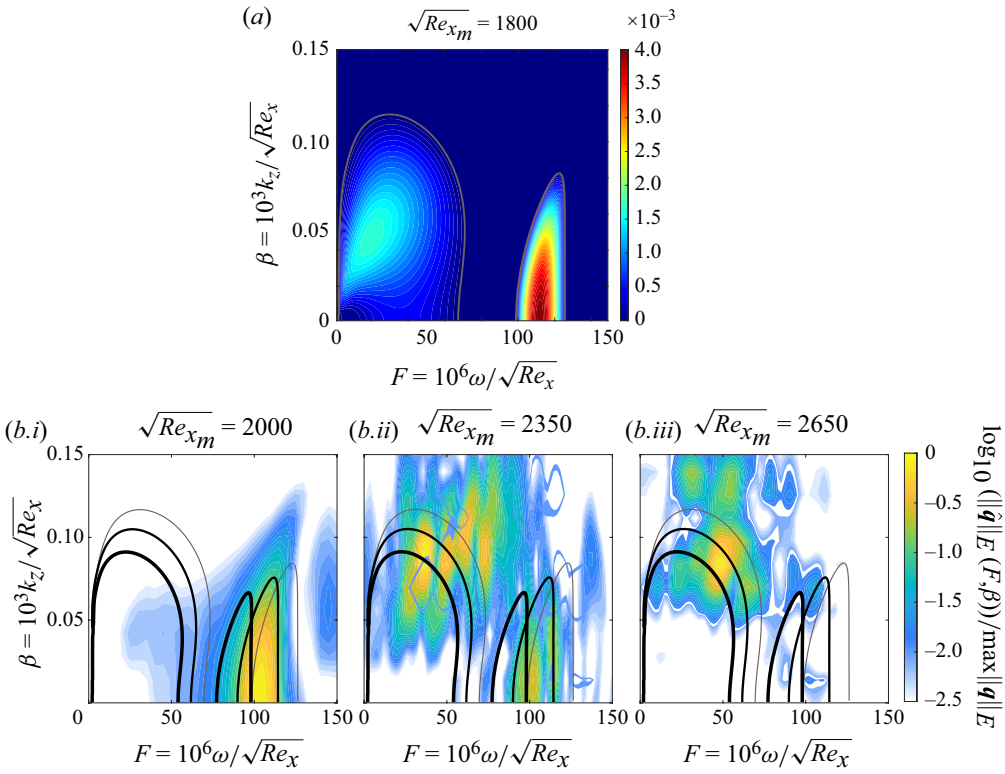


Figure 16. (a) The spatial growth rate of the most unstable LST mode in the wavenumber–frequency space at  $\sqrt{Re_x} = 1800$ . The black line marks the neutral curve. (b) The coloured contour shows the logarithmic of the normalised adjoint energy in the wavenumber–frequency space. Thin to thick lines show the spatial neutral curves for parallel flow at  $\sqrt{Re_x} = \{1800, 2000, 2350\}$ , plotted in the three panels, respectively.

within the neutral curves. The most energetic adjoint is recorded at  $(F, \beta) = (100, 0)$ , within the neutral curve for  $\sqrt{Re_x} = 2000$ . For the sensor located at  $\sqrt{Re_x} = 2350$ , within the transitional regime, the adjoint fields exhibit energy in wavenumbers beyond the neutral curve, or decaying modes, that are generated due to the spectral content of the turbulence of the forward base flow. This effect is more pronounced for the adjoint field starting from the sensor located at  $\sqrt{Re_x} = 2650$ , with most of the energy contained around  $(F, \beta) \approx (50, 0.1)$ .

In figure 17(a), we plot the eigenfunctions of the most unstable mode of the forward and adjoint spatial linear-stability operators, at the inflow plane  $\sqrt{Re_x} = 1800$  and  $(F, \beta) = (100, 0)$ . Similar to the temporal problem discussed in § 3.1, the adjoint mode has its largest amplitude in the adjoint velocity, and is concentrated near the boundary-layer edge. We will compare these eigen-stability profiles with the sensor DOD. When the adjoint fields from wall-pressure measurements at  $\sqrt{Re_{x_m}} = \{2000, 2350, 2650\}$  reach the inflow, they are Fourier transformed in time and in the span, and we plot the profiles at  $(F, \beta) = (100, 0)$  in figure 17(b). Each profile is normalised to unit energy, and they all show a strong dependence on the region near the edge of the boundary layer, with the only exception being the dependence on temperature which is also pronounced near the wall. Each of the profiles in figure 17(b) is in principle a superposition of discrete and

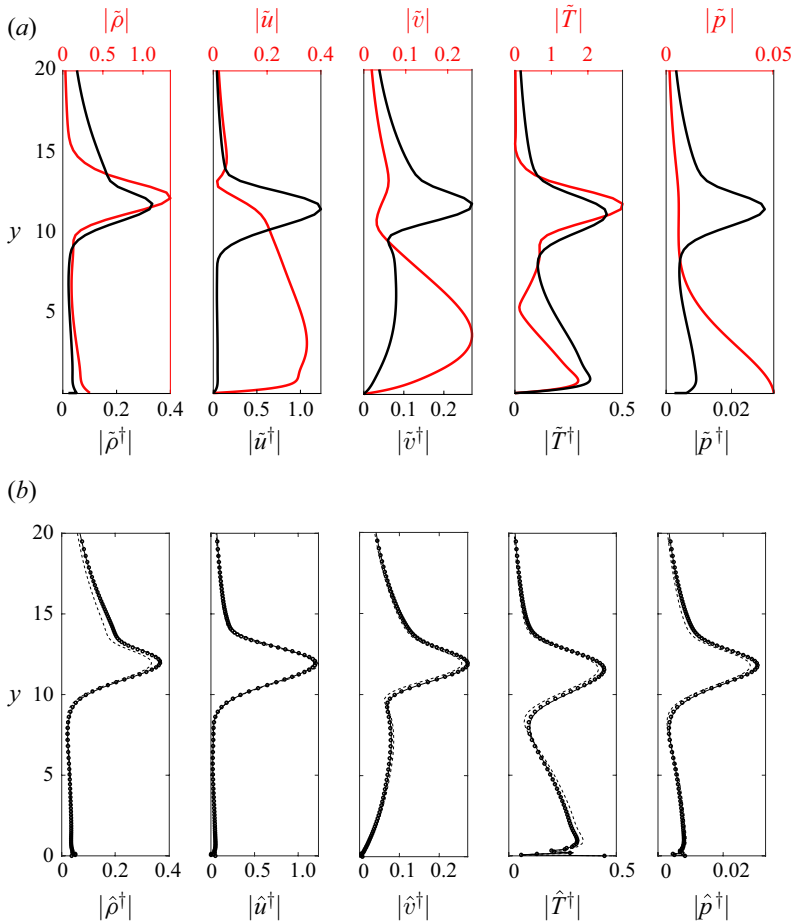


Figure 17. (a) Red lines show the most unstable forward eigen-modes from spatial LST results at  $(F, \beta) = (100, 0)$  with  $\sqrt{Re_x} = 1800$ . Black lines show the corresponding adjoint modes, defined using Chu's energy inner product. (b) The mode shapes of the adjoint fields at the inflow plane  $\sqrt{Re_x} = 1800$  from adjoint-Navier-Stokes simulation, case T. The adjoint mode is extracted at  $(F, \beta) = (100, 0)$ . Sensors are placed at  $\sqrt{Re_{x_m}} = 2000$  (black solid lines),  $\sqrt{Re_{x_m}} = 2350$  (black dashed lines) and  $\sqrt{Re_{x_m}} = 2650$  (symbols).

continuous eigenfunctions at this  $(F, \beta)$ . However, they are clearly dominated by the most unstable adjoint eigenfunction shown in figure 17(a). This agreement should, however, be viewed in context. We are here focusing on the boundary-layer portion of the DOD at an unstable  $(F, \beta)$  pair. Other wavenumbers are not included in this figure, in particular stable ones at large  $\beta$  which are the most energetic when  $\sqrt{Re_{x_m}} = 2650$  (figure 17) and are strongly influenced by the turbulence in the forward field.

In summary, the results demonstrate that wall-pressure measurements within the early turbulent region retain strong dependence on the upstream second-mode instability waves. The capacity of turbulence to obfuscate the interpretation of the measurements is primarily related to larger spanwise wavenumbers, beyond the unstable range. It is also important to once again underscore that a portion of the DOD of a wall-pressure measurement is the acoustic free-stream propagating wave, which was discussed in detail in the previous section.

#### 4. Conclusion

High-speed transitional boundary layers are sensitive to the disturbance environment which can quantitatively and qualitatively alter the transition mechanism. Assimilation of sensor data in numerical simulations is a rigorous and objective approach to augment the measurements and to discover the flow field that optimally reproduces the observations. Naturally, the success of data assimilation hinges on the properties of the available measurements, which we study using the notion of the DOD of a measurement probe. Put simply, the DOD captures when, where and what perturbations can affect the sensor. Physically, it is defined, at a time that precedes the measurement, as the region in space and the type of perturbation that will maximally impact the sensor signal at the measurement time. Mathematically, it is computed using the adjoint Navier–Stokes equations, starting from a measurement kernel and evolving it back in time in order to determine the sensor dependence on earlier disturbances at remote regions in the flow. Upstream flow events that are outside the DOD of the measurement kernel or are orthogonal to the adjoint field are entirely cloaked to the sensor. Those that are aligned with the adjoint field, through their forward evolution, have the largest linear impact on the measurement at the sensor location and observation time. We have also demonstrated how the definition of this adjoint field can be related to ideas from LST, so that existing tools from the community can be adapted and adopted to compute a sensor DOD.

The ideas introduced in this work were applied to a canonical flat-plate, zero-pressure-gradient, boundary-layer flow at Mach 4.5. Two configurations were considered: the first is a parallel and laminar base flow and the second is a spatial transitional case where the boundary layer is forced at the inflow by a superposition of instability waves and undergoes breakdown to turbulence. In all cases, we placed our focus on the DOD of a wall-pressure measurement, and in the spatial case we compared the domains of dependence of measurements in the laminar, transitional and turbulent regions of the flow.

In laminar boundary layers, whether they are parallel or spatially developing, the adjoint field from the wall-pressure sensor advects towards the edge of this boundary layer and splits into two sub-domains: the first advects upstream along the boundary layer, has its maximum energy near the boundary-layer edge and amplifies exponentially in backward time. During this back-in-time evolution, this portion progressively converges onto the leading eigenfunction of the adjoint linear-stability operator. The second portion of the adjoint field is emitted into the free stream, and propagates as an acoustic wave at the Mach angle. This part constitutes a considerable portion, up to approximately 40 % of the total adjoint energy at this stage of the evolution, and underscores that incident acoustic waves can have an appreciable impact of the measurement.

When the sensor is placed downstream of transition, in the turbulent boundary layer, its DOD retains the same two features discussed for sensors in the laminar region. However, the measurement sensitivity to the second mode is small compared with the dependence on high wavenumbers that are generated by the turbulence. In addition, as the adjoint travels back in time, it undergoes an appreciable change across the transition zone where it becomes significantly larger in streamwise extent, which indicates that the sensor becomes sensitive to a much larger region in space within a short time interval, followed by amplification in the laminar region.

The ideas explored here are relevant to understanding how the placement of a sensor in a high-speed flow can affect its DOD and, as a result, the accuracy of solving the data-assimilation problem. Analysis of the DOD adjoint field distinguishes the spectral components and types of disturbances that are observable by the sensor. These disturbances can therefore be discovered by a data-assimilation algorithm, and their

associated modal, non-modal and nonlinear mechanisms examined in detail. This work can also serve as a building block for the design of measurements. For example, these tools can be used to characterise and compare different types of measurements, and to optimise the placement of a group of sensors in a manner that maximises their collective DOD or that ensures overlap to reduce uncertainty.

**Acknowledgments.** The authors acknowledge Dr D. Buchta for the insightful discussions and sharing his computational expertise, and Mr C. Haas for careful reading of the paper.

**Funding.** The authors acknowledge financial support from the Air Force Office of Scientific Research (FA 9550-25-1-0011) and the Office of Naval Research (N 00014-25-1-2170).

**Declaration of interests.** The authors report no conflict of interest.

### Appendix A. Transformation between different adjoint definitions

In this appendix, the relationships between conserved and primitive variables are derived, both for the forward and adjoint problems. Since the transformations involve the forward-adjoint relations, we first reiterate that the adjoint field depends on the choice of inner product. Consider two vector fields  $\mathbf{f}$  and  $\mathbf{g}$  and the discrete representation of their inner product

$$(\mathbf{f}, \mathbf{g}) = \mathbf{f}^H \mathbf{W} \mathbf{g}, \tag{A1}$$

where  $\mathbf{W}$  is a weight matrix. For example, if the inner product represents spatial integration on a grid,  $(\mathbf{f}, \mathbf{g}) = \int_V \mathbf{f}^H \mathbf{g} dV = \mathbf{f}^H \mathbf{V} \mathbf{g}$ , we have  $\mathbf{W} = \mathbf{V}$  is a diagonal matrix with cell volumes as its elements. Using the same inner product in the forward-adjoint relation, we can write

$$(\mathcal{L} \mathbf{f}, \mathbf{g}) = (\mathbf{f}, \mathcal{L}^\dagger \mathbf{g}), \tag{A2}$$

where  $\mathcal{L}$  represents the forward operator associated with solving the linearised Navier–Stokes equations from  $t = 0$  to  $t = t_m$ , or  $\delta \mathbf{q}_{t_m} = \mathcal{L} \delta \mathbf{q}_0$ . We will use  $\mathcal{L}$  to refer to both the continuous operator and its discrete representation, and we will similarly overload the notation for the adjoint operators. The corresponding discrete representation of the adjoint with a general weight matrix  $\mathbf{W}$  can be derived as

$$\mathbf{f}^H \mathcal{L}^H \mathbf{W} \mathbf{g} = \mathbf{f}^H \mathbf{W} \mathcal{L}^\dagger \mathbf{g}, \tag{A3}$$

and as such

$$\mathcal{L}^\dagger = \mathbf{W}^{-1} \mathcal{L}^H \mathbf{W}, \tag{A4}$$

which is the relation between adjoint and Hermitian transpose. Equation (A4) captures that the adjoint operator and field depend on the weight matrix, and hence on the definition of the inner product.

The same relation can be used to derive the sought transformations. As an example, we will relate the adjoint operators and variables computed from energy and vector inner products. We will denote the respective operators as  $\mathcal{L}^\dagger$  and  $\mathcal{L}^\ddagger$ , and the associated weight matrices as  $\mathbf{W}_E$  and  $\mathbf{W}_2$ . The discrete representation of the adjoint operators can be written as

$$\mathcal{L}^\dagger = \mathbf{W}_E^{-1} \mathcal{L}^H \mathbf{W}_E, \quad \mathcal{L}^\ddagger = \mathbf{W}_2^{-1} \mathcal{L}^H \mathbf{W}_2, \tag{A5}$$

and therefore the transformation between  $\mathcal{L}^\dagger$  and  $\mathcal{L}^\ddagger$  is given by

$$\mathcal{L}^\dagger = \mathbf{W}_E^{-1} \mathbf{W}_2 \mathcal{L}^\ddagger \mathbf{W}_2^{-1} \mathbf{W}_E. \tag{A6}$$

From the above expression, the transformation between different adjoint variables, e.g.  $\mathbf{q}_0^\dagger = \mathcal{L}^\dagger \mathbf{q}_{t_m}^\dagger$  and  $\mathbf{q}_0^\ddagger = \mathcal{L}^\ddagger \mathbf{q}_{t_m}^\ddagger$  is given by

$$\mathbf{q}^\dagger = \mathbf{W}_E^{-1} \mathbf{W}_2 \mathbf{q}^\ddagger. \tag{A7}$$

Where  $\mathbf{W}_E = \mathbf{V} \boldsymbol{\Xi}$  is the energy inner product and  $\mathbf{W}_2 = \mathbf{V}$  is vector field inner product, we obtain the relation between these two adjoints

$$\mathbf{q}^\dagger = \boldsymbol{\Xi}^{-1} \mathbf{q}^\ddagger. \tag{A8}$$

In addition, for different choices of the forward state vector, the adjoint variables have different interpretations. The most common example is the adjoint associated with primitive variables  $\delta \mathbf{q} = [\delta \rho, \delta u, \delta v, \delta w, \delta T]^\top$  and with conserved ones  $\delta \mathbf{s} = [\delta \rho, \delta(\rho u), \delta(\rho v), \delta(\rho w), \delta E]^\top$ . The transformation between these two representations of the forward state is

$$\begin{bmatrix} \delta \rho \\ \delta(\rho u) \\ \delta(\rho v) \\ \delta(\rho w) \\ \delta E \end{bmatrix} = \begin{bmatrix} 1 & 0 & 0 & 0 & 0 \\ u & \rho & 0 & 0 & 0 \\ v & 0 & \rho & 0 & 0 \\ w & 0 & 0 & \rho & 0 \\ \frac{RT}{(\gamma-1)} + \frac{1}{2}(u^2 + v^2 + w^2) & \rho u & \rho v & \rho w & \frac{R\rho}{(\gamma-1)} \end{bmatrix} \begin{bmatrix} \delta \rho \\ \delta u \\ \delta v \\ \delta w \\ \delta T \end{bmatrix}, \tag{A9}$$

and

$$\begin{bmatrix} \delta \rho \\ \delta u \\ \delta v \\ \delta w \\ \delta T \end{bmatrix} = \begin{bmatrix} 1 & 0 & 0 & 0 & 0 \\ -u/\rho & 1/\rho & 0 & 0 & 0 \\ -v/\rho & 0 & 1/\rho & 0 & 0 \\ -w/\rho & 0 & 0 & 1/\rho & 0 \\ -\frac{\gamma-1}{R} \frac{E}{\rho^2} + \frac{\gamma-1}{R} \frac{u^2+v^2+w^2}{\rho} & -\frac{\gamma-1}{R} u/\rho & -\frac{\gamma-1}{R} v/\rho & -\frac{\gamma-1}{R} w/\rho & \frac{\gamma-1}{R} / \rho \end{bmatrix} \begin{bmatrix} \delta \rho \\ \delta(\rho u) \\ \delta(\rho v) \\ \delta(\rho w) \\ \delta E \end{bmatrix}. \tag{A10}$$

For compactness, we introduce the notation  $\delta \mathbf{q} = \mathcal{T} \delta \mathbf{s}$ , where  $\mathcal{T}$  is the transformation matrix in (A10).

We denote the forward linearised Navier–Stokes operators that advance  $\delta \mathbf{q}$  and  $\delta \mathbf{s}$  as  $\mathcal{L}_q$  and  $\mathcal{L}_s$ , respectively. The perturbation at time  $t_m$ , expressed in primitive form, can be evaluated by advancing an initial perturbation

$$\delta \mathbf{q}_{t_m} = \mathcal{L}_q \delta \mathbf{q}_0. \tag{A11}$$

Alternatively, the same final state can be reached starting from an initial disturbance in conservative form and then applying the transformation  $\mathcal{T}$

$$\delta \mathbf{q}_{t_m} = \mathcal{T} \mathcal{L}_s \delta \mathbf{s}_0 = \mathcal{T} \mathcal{L}_s \mathcal{T}^{-1} \delta \mathbf{q}_0. \tag{A12}$$

Comparing the above two equations, the transformation across operators is

$$\mathcal{L}_q = \mathcal{T} \mathcal{L}_s \mathcal{T}^{-1}. \tag{A13}$$

We now combine the above two transformations, the one that relates energy and vector products and the relation between conserved and primitive variables. This step is useful when comparing modes from LST and direct numerical simulations, for example. We start

from the forward-adjoint relations

$$\langle \mathcal{L}_q \delta \mathbf{q}_0, \mathbf{q}_{t_m}^\dagger \rangle = \langle \delta \mathbf{q}_0, \mathcal{L}_q^\dagger \mathbf{q}_{t_m}^\dagger \rangle, \quad [\mathcal{L}_s \delta \mathbf{s}_0, \mathbf{s}_{t_m}^\ddagger] = [\delta \mathbf{s}_0, \mathcal{L}_s^\ddagger \mathbf{s}_{t_m}^\ddagger]. \quad (\text{A14})$$

Angle brackets represent the energy inner product as in the main text, and the square brackets represent the dot product with spatial integration, which is often adopted in numerical simulations

$$(\mathbf{f}, \mathbf{g}) = \mathbf{f}^H \mathbf{V} \boldsymbol{\Xi} \mathbf{g}, \quad [\mathbf{f}, \mathbf{g}] = \mathbf{f}^H \mathbf{V} \mathbf{g}. \quad (\text{A15})$$

Therefore

$$\begin{aligned} \langle \mathcal{L}_q \delta \mathbf{q}_0, \mathbf{q}_{t_m}^\dagger \rangle &= \langle \mathcal{T} \mathcal{L}_s \mathcal{T}^{-1} \delta \mathbf{q}_0, \mathbf{q}_{t_m}^\dagger \rangle \\ &= (\mathcal{T} \mathcal{L}_s \mathcal{T}^{-1} \delta \mathbf{q}_0)^H \mathbf{V} \boldsymbol{\Xi} \mathbf{q}_{t_m}^\dagger \\ &= \delta \mathbf{q}_0^H (\mathbf{V} \boldsymbol{\Xi}) (\mathbf{V} \boldsymbol{\Xi})^{-1} (\mathcal{T} \mathcal{L}_s \mathcal{T}^{-1})^H (\mathbf{V} \boldsymbol{\Xi}) \mathbf{q}_{t_m}^\dagger \\ &= \left\langle \delta \mathbf{q}_0, \underbrace{(\mathbf{V} \boldsymbol{\Xi})^{-1} (\mathcal{T} \mathcal{L}_s \mathcal{T}^{-1})^H (\mathbf{V} \boldsymbol{\Xi})}_{\mathcal{L}_q^\dagger} \mathbf{q}_{t_m}^\dagger \right\rangle. \end{aligned} \quad (\text{A16})$$

We can then derive the relation between the two adjoint operators

$$\begin{aligned} \mathcal{L}_q^\dagger &= (\mathbf{V} \boldsymbol{\Xi})^{-1} (\mathcal{T} \mathcal{L}_s \mathcal{T}^{-1})^H (\mathbf{V} \boldsymbol{\Xi}) \\ &= (\mathbf{V} \boldsymbol{\Xi})^{-1} \mathcal{T}^H \mathcal{L}_s^H \mathcal{T}^H (\mathbf{V} \boldsymbol{\Xi}) \\ &= (\mathbf{V} \boldsymbol{\Xi})^{-1} \mathcal{T}^H \mathbf{V} \underbrace{\mathbf{V}^{-1} \mathcal{L}_s^H \mathbf{V}}_{\mathcal{L}_s^\ddagger} \mathbf{V}^{-1} \mathcal{T}^H (\mathbf{V} \boldsymbol{\Xi}) \\ &= (\mathbf{V} \boldsymbol{\Xi})^{-1} \mathcal{T}^H \mathbf{V} \mathcal{L}_s^\ddagger \mathbf{V}^{-1} \mathcal{T}^H (\mathbf{V} \boldsymbol{\Xi}). \end{aligned} \quad (\text{A17})$$

In order to obtain the transformation between the adjoint variables  $\mathbf{q}^\dagger$  and  $\mathbf{s}^\ddagger$ , we start from the adjoint equation  $\mathbf{q}_0^\dagger = \mathcal{L}_q^\dagger \mathbf{q}_{t_m}^\dagger$  and substitute the above expression for  $\mathcal{L}_q^\dagger$ , which yields

$$\mathbf{q}^\dagger = (\mathbf{V} \boldsymbol{\Xi})^{-1} \mathcal{T}^H \mathbf{V} \mathbf{s}^\ddagger. \quad (\text{A18})$$

The above expression relates the adjoint-primitive variables derived using the energy inner product and the adjoint-conserved variables derived using the vector inner product. Written explicitly, the transformation is given by

$$\begin{bmatrix} \rho \\ u \\ v \\ w \\ T \end{bmatrix}^\dagger = \boldsymbol{\Xi}^{-1} \begin{bmatrix} 1 & u & v & w & \frac{RT}{\gamma-1} + \frac{1}{2}(u^2 + v^2 + w^2) \\ 0 & \rho & 0 & 0 & \rho u \\ 0 & 0 & \rho & 0 & \rho v \\ 0 & 0 & 0 & \rho & \rho w \\ 0 & 0 & 0 & 0 & \frac{R\rho}{\gamma-1} \end{bmatrix} \begin{bmatrix} \rho \\ \rho u \\ \rho v \\ \rho w \\ E \end{bmatrix}^\ddagger$$

$$= 2 \begin{bmatrix} \frac{\bar{\rho}}{RT} & \frac{\bar{\rho}}{RT}u & \frac{\bar{\rho}}{RT}v & \frac{\bar{\rho}}{RT}w & \frac{\bar{\rho}T}{(\gamma-1)T} + \frac{\bar{\rho}}{2RT}(u^2 + v^2 + w^2) \\ 0 & \rho/\bar{\rho} & 0 & 0 & \rho u/\bar{\rho} \\ 0 & 0 & \rho/\bar{\rho} & 0 & \rho v/\bar{\rho} \\ 0 & 0 & 0 & \rho/\bar{\rho} & \rho w/\bar{\rho} \\ 0 & 0 & 0 & 0 & \rho T/\bar{\rho} \end{bmatrix} \begin{bmatrix} \rho \\ \rho u \\ \rho v \\ \rho w \\ E \end{bmatrix}^\ddagger. \quad (\text{A19})$$

### Appendix B. Validation of forward-adjoint duality

In the main text, we used adjoint techniques to compute the DOD of a sensor. We also evaluated the forward evolution of the adjoint field, to demonstrate how it leads to a variation at the sensor location and at the measurement time  $t_m$ . We remarked that disturbances outside the support of the adjoint field cannot result in a signal at the sensor location and time, and that a disturbance within the support of the adjoint field can still be unobservable by the sensor if it is orthogonal to  $\mathbf{q}_0^\ddagger$ . The former condition is straightforward, and the latter will be demonstrated in this appendix which also provides a demonstration and validation of forward-adjoint duality

$$\delta m = \left\langle \left( \frac{\partial \mathcal{M}}{\partial \mathbf{q}} \right)_{t_m}, \mathcal{L}_q \delta \mathbf{q}_0 \right\rangle = \left\langle \mathbf{q}_0^\ddagger, \delta \mathbf{q}_0 \right\rangle. \quad (\text{2.18})$$

We consider a parallel boundary layer at  $Re_x = 2000$  (case  $P$ ), and a wall-pressure measurement recoded by a sensor at  $(x_m, y_m, z_m) = (300, 0, 150)$  and  $t_m = 225$ . To evaluate the DOD of the sensor, we perform adjoint Navier–Stokes simulations starting from the measurement kernel, and obtain the adjoint field  $\mathbf{q}_0^\ddagger$ . We then verify duality, and thus validate our adjoint computation, by considering two types of disturbances that are both initialise in the free stream within the spatial support of the adjoint field, at  $(x_0, y_0, z_0) = (100, 40, 150)$ . The first disturbance is acoustic, and is constructed directly from the adjoint field according to

$$\delta \mathbf{q}_0 = G(\mathbf{x}) \mathbf{q}_0^\ddagger, \quad (\text{B1})$$

where  $G$  is a narrow Gaussian

$$G(\mathbf{x}) = \frac{1}{(2\pi\sigma^2)^{3/2}} e^{-\frac{\|\mathbf{x}-\mathbf{x}_0\|^2}{2\sigma^2}}. \quad (\text{B2})$$

The second disturbance is entropic, and is created according to

$$\delta \rho_0 = G(\mathbf{x}), \quad \delta u_0 = \delta v_0 = \delta w_0 = \delta p_0 = 0, \quad \delta T_0 = -\frac{\bar{T}}{\bar{\rho}} \delta \rho_0 = -\frac{\bar{T}}{\bar{\rho}} G(\mathbf{x}). \quad (\text{B3})$$

The forward evolutions of both disturbances were computed using the linearised Navier–Stokes equations, and are shown in figure 18(a,c). The acoustic disturbance emits waves that reach the boundary layer, and result in a measurable signal at the sensor location at  $t_m = 225$ . In contrast, the entropic disturbance, which is orthogonal to the adjoint field, is simply advected in the free stream with limited diffusion at the present Reynolds number. This disturbance does not penetrate the boundary layer, and leaves the sensor measurement unperturbed.

According to the forward-adjoint relation (2.18), the variation in the measurement  $\delta m$  can be evaluated either from the forward simulation and observing the variation in the pressure at the sensor,  $\delta m = \delta p(\mathbf{x}_m)|_{t_m}$ , or by performing the inner product of the adjoint field with the initial disturbance,  $\delta m = \langle \mathbf{q}_0^\ddagger, \delta \mathbf{q}_0 \rangle$ . In the linear limit, these two

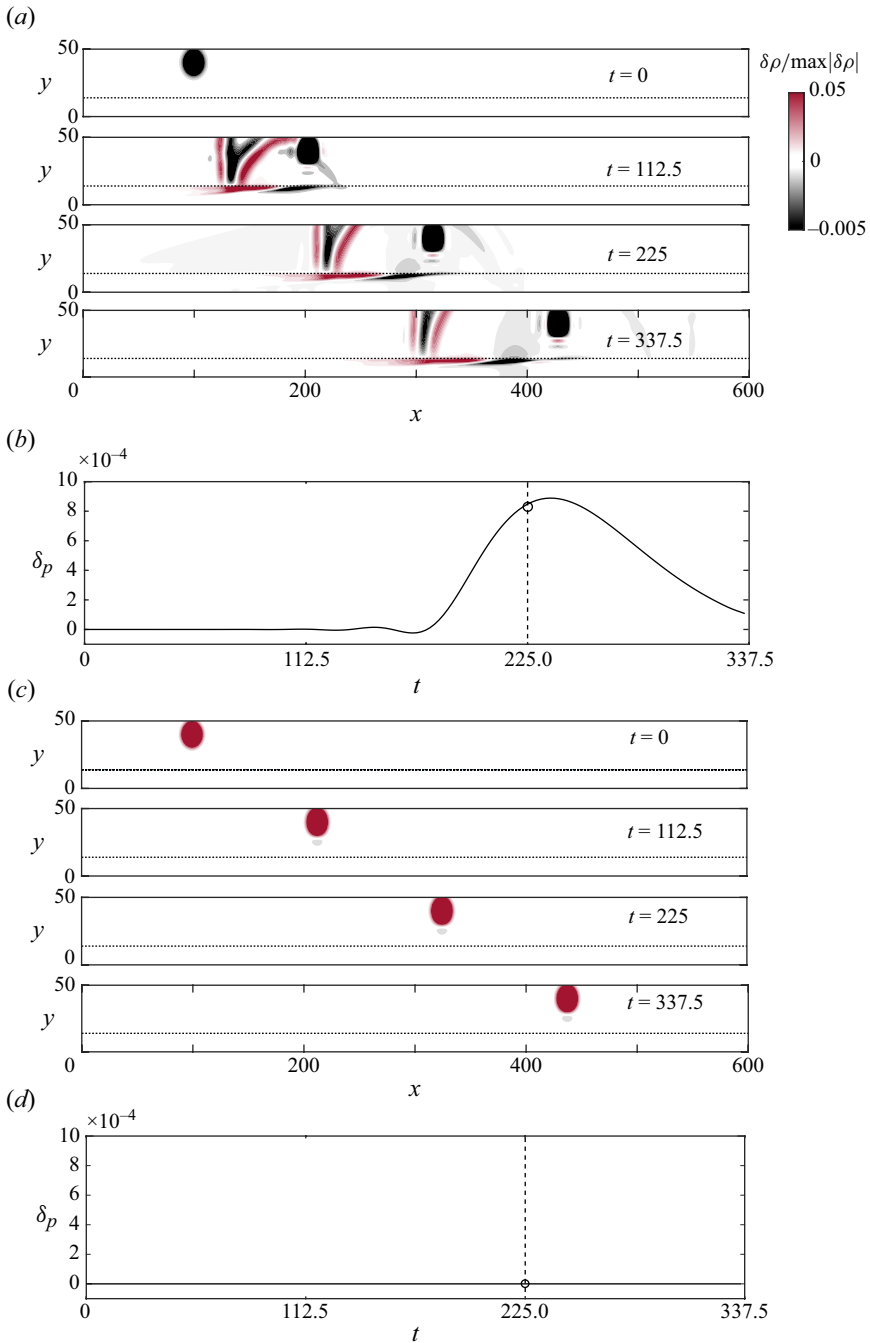


Figure 18. Examples of observable and unobservable initial disturbances, both within the spatial support of the sensor DOD. (a,c) Side views at  $z = 150$ , with contours showing the linearised Navier–Stokes evolution of a free-stream (a) acoustic and (c) entropic disturbance, both initiated at  $y = 40$  within the spatial support of the DOD. The entropic disturbance is, however, orthogonal to the adjoint fields  $p_0^\dagger$ . Contours are the normalised density  $\delta\rho/\max|\delta\rho|$ , and multiple times relative to the measurements at  $t_m = 225$ . (b,d) Wall-pressure signal at the sensor location, evaluated using (solid line) a forward linearised Navier–Stokes computation and (o) the inner product  $\langle \mathbf{q}_0^\dagger, \mathbf{q}_0 \rangle$ .

approaches should be mathematically equivalent and computationally equal to within machine precision

$$\delta p(\mathbf{x}_m)|_{t_m} = \langle \mathbf{q}_0^\dagger, \delta \mathbf{q}_0 \rangle. \quad (\text{B4})$$

The two approaches are compared in figure 18(b,d). The lines are the wall-pressure signals at the sensor locations as a function of time, which clearly demonstrates that only the free-stream acoustic disturbance is observable. The measurement time is marked by the dashed vertical lines, and the black circles are the values of the inner products  $\langle \mathbf{q}_0^\dagger, \delta \mathbf{q}_0 \rangle$ . The relative difference between the two approaches to computing  $\delta m$  is of the order of  $10^{-15}$ , which is consistent with machine error for double-precision arithmetic, thus validating the accuracy of the adjoint computation.

#### REFERENCES

- ASCH, M., BOCQUET, M. & NODET, M. 2016 *Data assimilation: methods, algorithms, and applications*. SIAM.
- BERRIDGE, D.C., KOSTAK, H., MCKIERNAN, G., WHEATON, B.M., WOLF, T.D. & SCHNEIDER, S.P. 2019 Hypersonic ground tests with high-frequency instrumentation in support of the boundary layer transition (BOLT) flight experiment. In AIAA Scitech 2019 Forum, p. 0090. American Institute of Aeronautics and Astronautics (AIAA).
- BERTOLOTTI, F.P., HERBERT, T. 1991 Analysis of the linear stability of compressible boundary layers using the PSE. *Theor. Comput. Fluid Dyn.* **3** (2), 117–124.
- BUCHTA, D.A., LAURENCE, S.J. & ZAKI, T.A. 2022 Assimilation of wall-pressure measurements in high-speed flow over a cone. *J. Fluid Mech.* **947**, R2.
- BUCHTA, D.A. & ZAKI, T.A. 2021 Observation-infused simulations of high-speed boundary-layer transition. *J. Fluid Mech.* **916**, A44.
- BUTLER, C.S. & LAURENCE, S.J. 2021 Interaction of second-mode disturbances with an incipiently separated compression-corner flow. *J. Fluid Mech.* **913**, R4.
- BUTLER, C.S. & LAURENCE, S.J. 2022 Transitional hypersonic flow over slender cone/flare geometries. *J. Fluid Mech.* **949**, A37.
- CHANG, C.-L., MALIK, M., ERLEBACHER, G. & HUSSAINI, M. 1991 Compressible stability of growing boundary layers using parabolized stability equations, In 22nd Fluid Dynamics, Plasma Dynamics and Lasers Conference, p. 1636. American Institute of Aeronautics and Astronautics (AIAA).
- CHANG, C.-L., MALIK, M.R., ERLEBACHER, G. & HUSSAINI, M.Y. 1993 Linear and nonlinear PSE for compressible boundary layers. Tech. Rep. Institute for Computer Applications in Science and Engineering, NASA Langley Research Center.
- CHU, B.-T. 1965 On the energy transfer to small disturbances in fluid flow (Part I). *Acta Mech.* **1** (3), 215–234.
- DI LEONI, C., PATRICIO, A., KARUNA, Z., TAMER, A., MENEVEAU, C. & KATZ, J. 2023 Reconstructing turbulent velocity and pressure fields from under-resolved noisy particle tracks using physics-informed neural networks. *Exp. Fluids* **64** (5), 95.
- CORCOS, G.M. 1963 Resolution of pressure in turbulence. *J. Acoust. Soc. Am.* **35** (2), 192–199.
- DU, Y., WANG, M. & ZAKI, T.A. 2023 State estimation in minimal turbulent channel flow: a comparative study of 4DVar and PINN. *Intl J. Heat Fluid Flow* **99**, 109073.
- DUAN, L., NICHOLSON, G.L., HUANG, J., CASPER, K.M., WAGNILD, R. & BITTER, N. 2019 Direct numerical simulation of nozzle-wall pressure fluctuations in a Mach 8 wind tunnel. In AIAA Scitech 2019 Forum, pp. 0874.
- FEDOROV, A. 2011 Transition and stability of high-speed boundary layers. *Annu. Rev. Fluid Mech.* **43** (1), 79–95.
- FEDOROV, A. & TUMIN, A. 2011 High-speed boundary-layer instability: old terminology and a new framework. *AIAA J.* **49** (8), 1647–1657.
- FRANKO, K.J. & LELE, S. 2014 Effect of adverse pressure gradient on high speed boundary layer transition. *Phys. Fluids* **26** (2), 024106.
- HADER, C. & FASEL, H.F. 2018 Towards simulating natural transition in hypersonic boundary layers via random inflow disturbances. *J. Fluid Mech.* **847**, R3.
- HADER, C. & FASEL, H.F. 2019 Direct numerical simulations of hypersonic boundary-layer transition for a flared cone: fundamental breakdown. *J. Fluid Mech.* **869**, 341–384.

- HANIFI, A., SCHMID, P.J. & HENNINGSON, D.S. 1996 Transient growth in compressible boundary layer flow. *Phys. Fluids* **8** (3), 826–837.
- HOFFERTH, J.W. & OGG, D.R. 2019 Reactivation of VKF wind tunnel D by AFRL at AEDC: supersonic performance and freestream characterizations. In AIAA Aviation 2019 Forum, pp. 2856.
- JAHANBAKHSI, R. & ZAKI, T.A. 2019 Nonlinearly most dangerous disturbance for high-speed boundary-layer transition. *J. Fluid Mech.* **876**, 87–121.
- KENNEDY, R.E., JEWELL, J.S., PAREDES, P. & LAURENCE, S.J. 2022 Characterization of instability mechanisms on sharp and blunt slender cones at Mach 6. *J. Fluid Mech.* **936**, A39.
- KENNEDY, R.E., LAURENCE, S.J., SMITH, M.S. & MARINEAU, E.C. 2018 Investigation of the second-mode instability at Mach 14 using calibrated schlieren. *J. Fluid Mech.* **845**, R2.
- KIMMEL, R.L., BORG, M.P., JEWELL, J.S., LAM, K.-Y., BOWERSOX, R.D., SRINIVASAN, R., FUCHS, S. & MOONEY, T. 2017 AFRL Ludwig tube initial performance, In 55th AIAA Aerospace Sciences Meeting, p. 0102. American Institute of Aeronautics and Astronautics (AIAA).
- KOCIAN, T., PEREZ, E., OLIVIERO, N., KUEHL, J. & REED, H. 2013 Hypersonic stability analysis of a flared cone. In 51st AIAA Aerospace Sciences Meeting Including the New Horizons Forum and Aerospace Exposition, p. 667. American Institute of Aeronautics and Astronautics (AIAA).
- KOSTAK, H., BOWERSOX, R.D., MCKIERNAN, G., THOME, J., CANDLER, G.V. & KING, R. 2019 Freestream disturbance effects on boundary layer instability and transition on the afosr BOLT geometry. In AIAA Scitech 2019 Forum, pp. 0088.
- KOSTAK, H.E. & BOWERSOX, R.D.W. 2021 Preflight ground test analyses of the boundary layer transition (BOLT) flight geometry. *J. Spacecr. Rockets* **58** (1), 67–77.
- KOVASZNAVY, L.S.G. 1953 Turbulence in supersonic flow. *J. Aeronaut. Sci.* **20** (10), 657–674.
- LAW, K., STUART, A. & ZYGALAKIS, K. 2015 *Data Assimilation*, vol. 214. Springer.
- LI, Y., ZHANG, J., DONG, G. & ABDULLAH, N.S. 2020 Small-scale reconstruction in three-dimensional Kolmogorov flows using four-dimensional variational data assimilation. *J. Fluid Mech.* **885**, A9.
- LOCKWOOD, B. & MAVRIPLIS, D. 2010 Parameter sensitivity analysis for hypersonic viscous flow using a discrete adjoint approach. In 48th AIAA Aerospace Sciences Meeting Including the New Horizons Forum and Aerospace Exposition, p. 447. American Institute of Aeronautics and Astronautics (AIAA).
- LOOSE, N. & HEIMBACH, P. 2021 Leveraging uncertainty quantification to design ocean climate observing systems. *J. Adv. Model. Earth Syst.* **13** (4), e2020MS002386. arXiv:<https://agupubs.onlinelibrary.wiley.com/doi/pdf/10.1029/2020MS002386>
- LUEPTOW, R.M. 1995 Transducer resolution and the turbulent wall pressure spectrum. *J. Acoust. Soc. Am.* **97** (1), 370–378.
- MACK, L.M. 1975 Linear stability theory and the problem of supersonic boundary-layer transition. *AIAA J.* **13** (3), 278–289.
- MACK, L.M. 1984 Boundary-layer linear stability theory. *Agard Rep.* **709** (3), 1–3.
- MALIK, M.R. & SPALL, R.E. 1991 On the stability of compressible flow past axisymmetric bodies. *J. Fluid Mech.* **228**, 443–463.
- MAMROL, D. & JEWELL, J.S. 2022 Freestream noise in the purdue university boeing/afosr Mach-6 quiet tunnel. In AIAA Scitech 2022 Forum, p. 2453. American Institute of Aeronautics and Astronautics (AIAA).
- MARINEAU, E.C., MORARU, G.C., LEWIS, D.R., NORRIS, J.D., LAFFERTY, J.F., WAGNILD, R.M. & SMITH, J.A. 2014 Mach 10 boundary layer transition experiments on sharp and blunted cones. In 19th AIAA International Space Planes and Hypersonic Systems and Technologies Conference, pp. 3108.
- MONS, V., CHASSAING, J.-C., GOMEZ, T. & SAGAUT, P. 2016 Reconstruction of unsteady viscous flows using data assimilation schemes. *J. Comput. Phys.* **316**, 255–280.
- MONS, V., DU, Y. & ZAKI, T.A. 2021 Ensemble-variational assimilation of statistical data in large-eddy simulation. *Phys. Rev. Fluids* **6** (10), 104607.
- MONS, V., WANG, Q. & ZAKI, T.A. 2019 Kriging-enhanced ensemble variational data assimilation for scalar-source identification in turbulent environments. *J. Comput. Phys.* **398**, 108856.
- MOYES, A. & REED, H.L. 2019 Nonlinear boundary-layer stability analysis of BOLT and HIFiRE-5. In AIAA Aviation 2019 Forum, pp. 2972.
- PARK, J. & ZAKI, T.A. 2019 Sensitivity of high-speed boundary-layer stability to base-flow distortion. *J. Fluid Mech.* **859**, 476–515.
- PARZIALE, N.J., SHEPHERD, J.E. & HORNUNG, H.G. 2014 Free-stream density perturbations in a reflected-shock tunnel. *Exp. Fluids* **55** (2), 1–10.
- POULAIN, A., CONTENT, C., RIGAS, G., GARNIER, E. & SIPP, D. 2024 Adjoint-based linear sensitivity of a supersonic boundary layer to steady wall blowing–suction/heating–cooling. *J. Fluid Mech.* **978**, A16.
- SCHNEIDER, S.P. 2015 Developing mechanism-based methods for estimating hypersonic boundary-layer transition in flight: the role of quiet tunnels. *Prog. Aerosp. Sci.* **72**, 17–29.

- STAMMER, D., BALMASEDA, M., HEIMBACH, P., KÖHL, A. & WEAVER, A. 2016 Ocean data assimilation in support of climate applications: status and perspectives. *Annu. Rev. Mar. Sci.* **8** (2016), 491–518.
- VISHNAMPET, R., BODONY, D.J. & FREUND, J.B. 2015 A practical discrete-adjoint method for high-fidelity compressible turbulence simulations. *J. Comput. Phys.* **285**, 173–192.
- VISHNAMPET GANAPATHI SUBRAMANIAN, R. 2015 An exact and consistent adjoint method for high-fidelity discretization of the compressible flow equations. Diss. University of Illinois at Urbana-Champaign.
- WANG, M., WANG, Q. & ZAKI, T.A. 2019 Discrete adjoint of fractional-step incompressible Navier–Stokes solver in curvilinear coordinates and application to data assimilation. *J. Comput. Phys.* **396**, 427–450.
- WANG, M. & ZAKI, T.A. 2021 State estimation in turbulent channel flow from limited observations. *J. Fluid Mech.* **917**, A9.
- WANG, Q., WANG, M. & ZAKI, T.A. 2022 What is observable from wall data in turbulent channel flow? *J. Fluid Mech.* **941**, A48.
- WHEATON, B.M., BERRIDGE, D.C., WOLF, T.D., ARAYA, D.B., STEVENS, R.T., MCGRATH, B.E., KEMP, B.L. & ADAMCZAK, D.W. 2021 Final design of the boundary layer transition (BOLT) flight experiment. *J. Spacecr. Rockets* **58** (1), 6–17.
- ZAKI, T.A. 2025 Turbulence from an observer perspective. *Annu. Rev. Fluid Mech.* **57** (1), 311–334.
- ZAKI, T.A. & WANG, M. 2021 From limited observations to the state of turbulence: fundamental difficulties of flow reconstruction. *Phys. Rev. Fluids* **6** (10), 100501.
- ZUCCHER, S., TUMIN, A. & RESHOTKO, E. 2006 Parabolic approach to optimal perturbations in compressible boundary layers. *J. Fluid Mech.* **556**, 189–216.